ACS OMEGA

Open Access

http://pubs.acs.org/journal/acsodf

Article

Calcium-Poison-Resistant Cu/$YCeO_2$−TiO_2 Catalyst for the Selective Catalytic Reduction of NO with CO and Naphthalene in the Presence of Oxygen

Josefina Herrera, Gonzalo Aguila, Ye Zhu, ZhiHang Xu, and Sichem Guerrero Ruz*

Cite This: *ACS Omega* 2024, 9, 40394−40410

Read Online

ACCESS | Metrics & More | Article Recommendations | Supporting Information

ABSTRACT: The pollution from industrial processes based on biomass combustion is still an ongoing problem. In the present contribution, the selective catalytic reduction of NO with CO and naphthalene is carried out in the presence of 10% oxygen. The accumulation of alkaline and alkaline earth metals during biomass combustion is here simulated by the addition of calcium to a Cu-impregnated $YCeO_2$−TiO_2 support. The results show that a high dispersion of copper is obtained, which is resistant to the accumulation of calcium. Full conversion of CO and naphthalene is achieved above 200 °C, whereas NO conversions of 80, 90, and 87% are obtained for the catalysts with Ca loadings of 2.6, 5.2, and 13%, respectively, at 350 °C. It is proposed that the high activity of the catalysts is ascribed to the formation of Cu−O_x−Ce species and that the accumulation of Ca acts as a barrier to avoid copper sintering. It was found that different forms of carbonate and nitrite/nitrate species form during reaction, coexisting as adsorbed species during the SCR reaction. The selectivity to N_2 was almost 100% in all cases, due to the small presence of NO_2 in the reactor outlet (no N_2O was detected in any conditions).

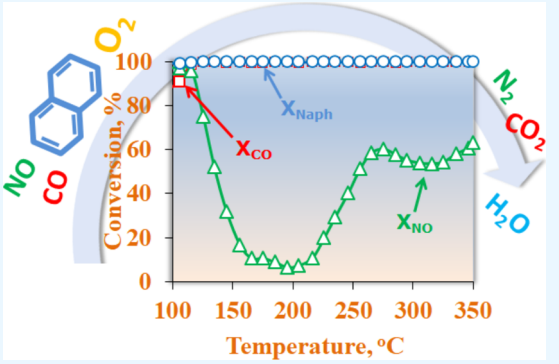

1. INTRODUCTION

According to the International Energy Outlook 2021 published by the Energy Information Administration, global energy consumption will increase by nearly 50% by 2050.[1] According to that report, approximately 100 million people may revert to the use of traditional biomass for cooking due to increasing price and economic pressure, making access to modern energy sources more difficult. This effect not only puts pressure in different ecosystems but also increases the generation of gaseous contaminants in the environment. The World Health Organization estimates that exposure to ambient and household pollution results in 6.7 million deaths per year and that those relying on polluting fuels and old technologies for cooking amount to 2.4 billion people.[2] The latter is especially important in developing countries where it is estimated that the amount of biomass converted into pollutants in simple stoves varies from 10% to 38%.[3] Some common health-affecting pollutants are carbon monoxide (CO), nitric oxides (NO_x), particulate matter (PM), volatile organic compounds (VOCs), and polycyclic aromatic hydrocarbons (PAHs), among others. The health-related problems associated with these pollutants may induce a variety of respiratory problems, ranging from infections and pulmonary diseases to carcinogenic, mutagenic, and teratogenic effects.[4−7] The elimination of these pollutants must take into account the complexities associated with each compound. For example, the catalytic reduction of NO into N_2 could be a plausible approach given that the reducing agent (H_2, CO, or other hydrocarbon present in the exhaust) is not first oxidized by the presence of oxygen, which is a problem because the exhaust is usually a lean mixture. In the case of COVs and PAHs, large molecules are difficult to oxidize, and they tend to accumulate as coal tar in the exhaust of the combustion chamber, forming an explosive mixture. On the other hand, particulate matter can be recovered in sufficiently fine filters, but this does not resolve the problem of gaseous pollutants. Thus, an ideal catalytic system should be able to reduce NO using CO or other hydrocarbons present in the mixture, and it should be able to oxidize large molecules along with being resistant to the accumulation of particulate matter on the catalyst surface. For example, methane acts as a reducer of NO in the presence of O_2 on a Ga/H-ZSM-5 catalyst, which was ascribed to a synergism between Ga and H^+ from the zeolite support.[8] However, water vapor present on the CH_4−NO−O_2 mixture strongly inhibits the catalyst due to site occupancy by H_2O on a Ga-ZSM-5 catalyst, whereas In-ZSM-5 is fairly active even in the presence of 10% steam.[9] Propene has also been

Received: March 12, 2024
Revised: September 9, 2024
Accepted: September 13, 2024
Published: September 21, 2024

demonstrated to be able to reduce NO in the presence of oxygen on a copper-exchanged zeolite, Cu-ZSM-5,[10,11] on Pt/Al_2O_3,[12,13] on Fe-PCH,[14] on Ag/Al_2O_3[15] and on Fe/β or Fe−Mn/β.[16,17] Additionally, ethane has reducing activity of NO on zeolite catalysts in the order Rh/ZSM-5 > ColZSM-5 > Cu/ZSM-5 ≫ Pt/ZSM-5.[18] Other hydrocarbons for the reduction of NO have also been studied, such as ethylene on Cu/Al-MCM-41,[19] propane on Fe/Al_2O_3/cordierite,[20] Cu-TNU-9,[21] Pt/$Ce_{1-x}Zr_xO_{2-\delta}$,[22] dodecane on Ag/Al_2O_3,[23] octane on Ag/Al_2O_3,[24] propylene on Pt/Al_2O_3,[25] and toluene on AuPd/TiO_2.[26] Regarding the use of PAHs as reducers of NO in the presence of oxygen, the reported literature is rather scarce, possibly due to the difficulty in selectively decomposing the reducer and using it as an NO reducer instead of fully oxidizing the reducer to CO_2 and water. Another factor is the recalcitrance character of PAHs, which are difficult to react under mild temperature conditions.[27] The smallest PAH molecule is naphthalene, and it is frequently used as a probe molecule due to its low toxicity, although it can cause the breakdown of red blood cells if ingested or inhaled in large quantities.[28] We previously reported that a K/Cu/$SmCeO_2$−TiO_2 catalyst was able to effectively use naphthalene and CO to reduce NO in the presence of oxygen.[29,30] The addition of potassium was used to simulate the presence on a working catalyst of alkali and alkaline earth metals, which naturally accumulate in biomass during its life-cycle and end up on the catalyst surface upon combustion. In a subsequent report, calcium was used instead of potassium to avoid potassium volatility.[31] Although it was found that a Ca/Cu/$YCeO_2$−TiO_2 catalyst was active in selectively reducing NO with naphthalene and CO, there are still pending questions regarding the role of Ca during the reaction. Regarding the use of CeO_2 as support, extensive research has been conducted on Cu/CeO_2 catalysts, including the Cu/$YCeO_2$, as documented in the literature.[32−36] Our group's investigations have focused on determining the optimal copper loading (or copper's dispersion capacity) across different supports, finding that CeO_2 can facilitate a copper content of approximately 8.4% per 100 m^2/g of CeO_2.[37] In Cu−Ce supported catalysts, the incorporation of Ce is found to increase the maximal dispersion capability of supports. For example, while the intrinsic copper dispersion limit of a ZrO_2 support is 4% Cu for every 100 m^2/g of ZrO_2, the presence of the Ce can increase this limit to around 11% Cu per 100 m^2/g of ZrO_2, demonstrating the crucial role of Ce in boosting the copper dispersion potential of supports.[38] In the present work, a $YCeO_2$−TiO_2-supported copper catalyst is used to investigate the role of Ca as it accumulates on the catalyst surface. The use of a TiO_2-supported CeO_2 ensemble points to favor a high dispersion of ceria before impregnation of copper and calcium, which can benefit the dispersion and interaction of both copper and calcium with the ceria support. The inclusion of yttrium added thermal stability to the cubic fluorite structure of CeO_2, which has been ascribed to the partial substitution of Ce^{4+} ions (0.97 Å) with large Y ions (1.02 Å),[39] giving thermal stability to this phase[40,41] and also promoting the presence of reactive oxygen species.[42,43] Proper characterization techniques are applied to understand the interaction of Ca with Cu during transient conditions of the catalyst applied to the reduction of NO with CO and naphthalene in the presence of oxygen. Transient conditions were used instead of equilibrium to subject the catalyst to harsh conditions where large amounts of pollutants are generated. In this unsteady condition the catalyst must resist poisoning and maintain a high activity eliminating the pollutants.

2. EXPERIMENTAL SECTION

A reverse micelle method was used to prepare the denoted $YCeO_2$−TiO_2 support. A mixture of a commercial surfactant (Tomadol 91−6, Air Products) and *n*-amyl alcohol (Merck), 62 and 38 w/w%, respectively, was added to 56 mL of isooctane and 80 mL of distilled water under stirring and at room temperature, obtaining a clear and stable solution. The added water contained dissolved cerium(III) nitrate hexahydrate and yttrium(III) nitrate hexahydrate (Sigma-Aldrich). The latter compound was added to increase the thermal stability of the final support and corresponded to 10% Y with respect to the amount of Ce. The as-received TiO_2 nanoparticles (Sigma-Aldrich) were added to the previous microemulsion. A second microemulsion was prepared containing only the surfactant, *n*-amyl alcohol, isooctane and water, with the latter diluting 6.5 mL of NH_3 (25%, Merck). This latter solution was added dropwise to the first microemulsion under strong stirring. The resulting precipitate was subjected to solvent extraction using hexane in a Gregar extractor for 6 h. The obtained $YCeO_2$−TiO_2 support was then dried and calcined at 500 °C for 3 h. Then, the active phases were added by incipient wetness impregnation of solutions containing the respective copper precursor or both copper and calcium precursors (metal w/w% loading: 2.6% Cu and 1.8% Ca, which were obtained by applying a central composite design to optimize these metal loadings[31]). The gradual accumulation of calcium on the catalyst surface was simulated by impregnating a Cu/$YCeO_2$−TiO_2catalyst (incipient wetness impregnation) with 1.8, 2.6, 5.2, and 13% (w/w%) of the calcium precursor (these amounts correspond to Ca metal loading and they fall in the range of accumulation of Ca that a working catalyst should experience). The final catalyst is hereafter referred to as XCa/Cu/$YCeO_2$−TiO_2, where *X* is the percent loading of calcium specifically used. For reference, a sample containing only copper was prepared and denoted as Cu/$YCeO_2$−TiO_2. The activity of the catalysts (0.42 g) was determined in a 1 cm I.D. plug-flow quartz reactor prior to calcination at 500 °C for 1 h in a flow of 10 cc/min of pure oxygen. The gaseous mixture consisted of 1% CO, 500 ppm of NO, and 10% O_2, balanced in He, flowing at 50 cc/min(GHSV = 10,000 h^{-1}). For the experiments studying the effect of the calcination temperature on the catalytic activity, the impregnated catalysts were loaded in the reactor and calcined in situ before reaction at 400, 450, 500, 550, or 600 °C. The outlet gases from the reactor were analyzed by an infrared spectrometer (Shimadzu, IRPrestige21) equipped with a 2.4 m Pike gas cell. A chromatograph (Series 580, Gow-Mac) equipped with a 60/80 molecular sieve 5A (Supelco) was also used. The conversion of CO and NO was calculated as follows

$$X_{CO}(\%) = (CO_{in} - CO_{out})/CO_{in} \times 100 \quad (1)$$

$$X_{NO}(\%) = (NO_{in} - NO_{out})/NO_{in} \times 100 \quad (2)$$

The latter conversion together with the calculation of N_2 selectivity was checked by using a mass spectrometer connected to the outlet of the reactor (OmniStar, Pfeiffer).

The surface area (BET) and pore size distribution of the various prepared samples were obtained from N_2 adsorption isotherms obtained in a physisorption analyzer Anton Paar, model Nova-600. BET area was obtained from the adsorption

https://doi.org/10.1021/acsomega.4c02423
ACS Omega 2024, 9, 40394−40410

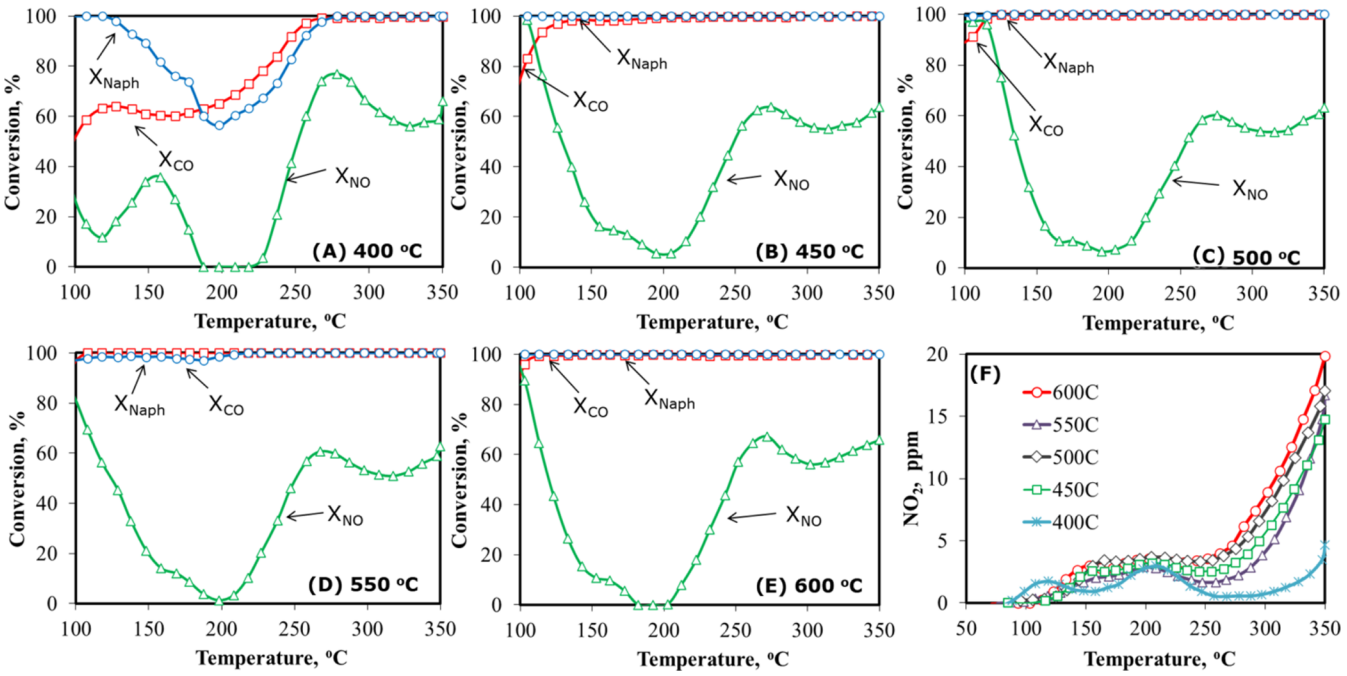

Figure 1. Activity on the selective reduction of NO with CO and naphthalene for the Ca/Cu/$YCeO_2$−TiO_2 catalyst calcined before reaction at: (A) 400 °C, (B) 450 °C, (C) 500 °C, (D) 550 °C, and (E) 600 °C. The presence of NO_2 at the exit of the reaction is shown in (F).

branch of the isotherm, whereas the density functional theory model was used for obtaining the pore size distribution. Before the analysis, the sample was outgassed at 200 °C for 2 h. Additionally, the samples were characterized by scanning transmission electron microscopy (STEM) in high angle annular dark field (HAADF) mode and transmission electron microscopy (TEM) using STEM/TEM (JEM-2100F, JEOL, Japan) combined with X-ray spectroscopy (EDX). Electron energy loss spectrum (EELS) was carried out by a Gatan Enfina electron spectrometer. Samples of each catalyst were additionally studied by temperature-programmed reduction (TPR) experiments in a 5% H_2/Ar stream using a 10 °C/min ramp. In these experiments, 0.1 g of catalyst was loaded into the reactor and oxidized in situ in a 20 cm^3/min stream of pure O_2 at 500 °C for 1 h. Diffuse reflectance infrared Fourier transform spectroscopy (DRIFTS) analyses were performed with an infrared spectrometer (Shimadzu, IRPrestige21) using a temperature-controlled stainless steel reactor (Pike) equipped with gas and refrigerant ports and a KBr window. The analyses parameters were Box-Car apodization, 100 scans per sample with a resolution of 4.0 cm^{-1}, using a DLATGS detector. In order to have similar conditions to those used in the activity tests, the loaded sample in the DRIFTS cell was subjected to calcination at 500 °C for 1 h in a flow of 10 cc/min of pure oxygen. For the operando experiments, the output of the DRIFTS cell and/or the reactor output was monitored by a mass spectrometer (OmniStar, Pfeiffer) under reaction conditions. Operando Raman spectra were recorded using a confocal Raman spectrometer (XploRA Plus, Horiba Scientific) to measure the structural changes during the reaction. This spectrometer was equipped with 532 and 785 nm lasers along with a temperature-controlled reactor cell (LINKAM). XPS was performed in a Surface Analysis Station 1, model RQ300/2, using monochromatic Al−Kα radiation ($h\nu$ = 1486.6 eV) at 15 kV and 10 mA and equipped with a DESA 150 detector. The binding energies were referenced to the C 1s peak at 284.6 eV. The samples were mounted on carbon tapes and no charge compensation was used in any case. For the analyses, Gaussian/Lorentzian line shapes were used with Shirley background and with no constraints.

3. RESULTS

3.1. Activity on the Selective Reduction of NO with CO and Naphthalene (in the Presence of O_2). Depending on the calcination temperature before reaction, the catalytic activity can depend on several factors, such as the degree of oxidation of the active phases, the aggregation of the active sites, the elimination of impurities from the impregnation steps, among others. For this reason, different calcination temperatures were explored before the reaction. In other words, the catalyst loaded in the reactor was calcined at a specific temperature, then cooled down to room temperature and the actual reaction started. The selected calcination temperatures were 400, 450, 500, 550, and 600 °C.

For the first part of this work, the 1.8Ca/Cu/$YCeO_2$-TiO_2 catalyst was selected to study the effect of in situ calcination at different temperatures before reducing NO with CO and naphthalene. As mentioned before, the loadings of calcium (1.8%) and copper (2.6%) were obtained from a previous work, and these amounts represent the optimum loadings of both metals.[31] Figure 1 shows the conversion of each pollutant with temperature after calcining the 1.8Ca/Cu/$YCeO_2$−TiO_2 catalyst prior to reaction at 400, 450, 500, 550, and 600 °C. It should be noted that physical adsorption of NO and naphthalene can occur at low temperature. We have previously reported that catalysts based on CeO_2 and TiO_2 are excellent adsorption materials, especially at low temperatures.[44,45] This means that rather than observing NO reduction with CO and naphthalene below 100 °C, instead, it is the physical adsorption of NO and naphthalene that occurs, and for this reason, the conversion curve for NO and naphthalene seems to be high below 100 °C, but instead, it truly represents that

https://doi.org/10.1021/acsomega.4c02423
ACS Omega 2024, 9, 40394−40410

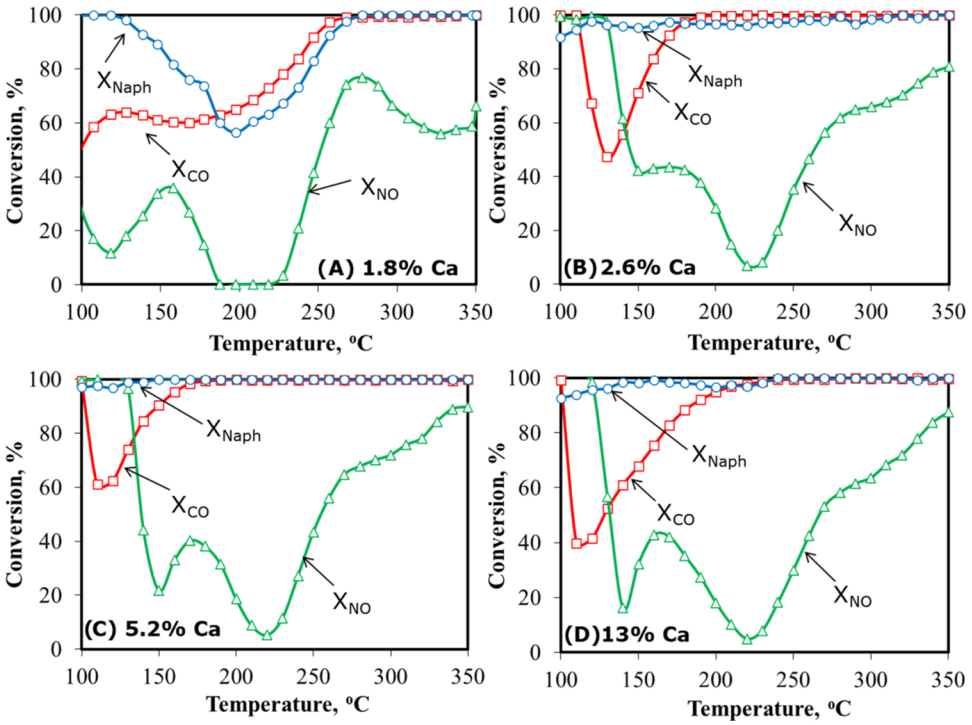

Figure 2. Activity on the selective reduction of NO with CO and naphthalene for the Ca/Cu/$YCeO_2$−TiO_2 catalysts with loading of Ca of (A) 1.8%, (B) 2.6%, (C) 5.2%, and (D) 13%. All samples were calcined at 450 °C before the reaction.

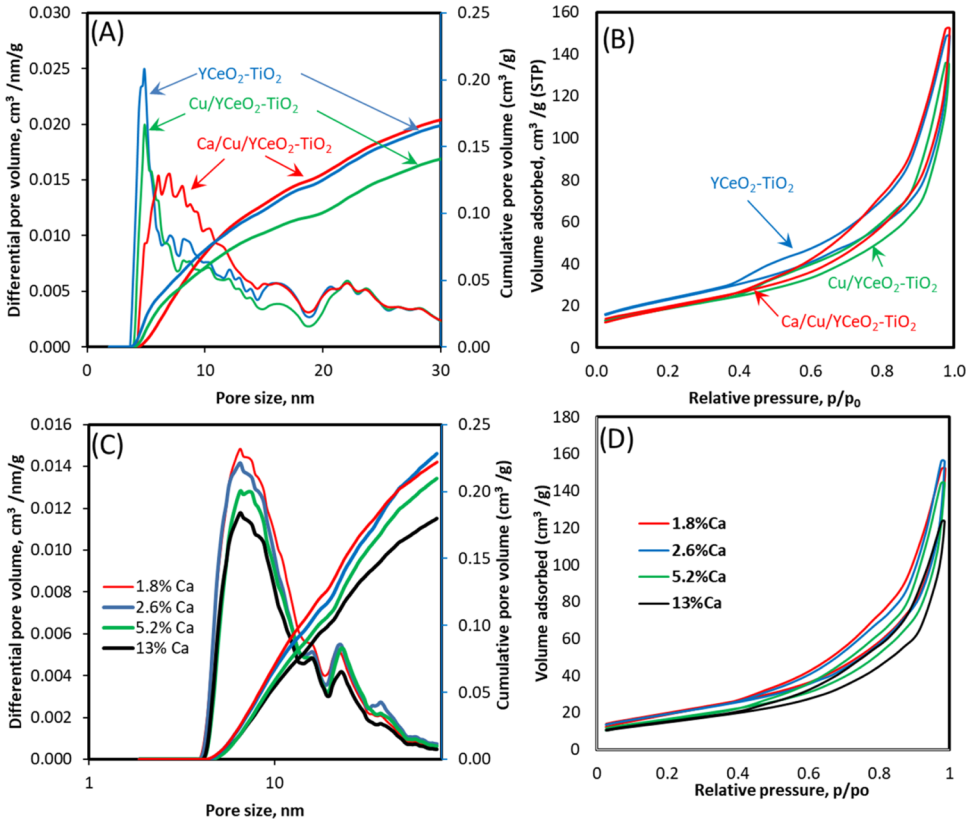

Figure 3. (A) Pore size distribution and (B) N_2 isotherms of the $YCeO_2$−TiO_2 support and Cu/$YCeO_2$−TiO_2 and Ca/$CuYCeO_2$−TiO_2 catalysts. (C) Pore size distribution and (D) N_2 isotherms for the Ca/$CuYCeO_2$−TiO_2 catalysts with different amounts of Ca: 1.8, 2.6, 5.2, and 13%.

either NO or naphthalene are being adsorbed on the sample and then both are released at higher temperatures, which is evident for NO conversion abruptly decreasing in the range of 100−200 °C in most cases. From 200 °C, the actual reduction reaction of NO with CO and naphthalene is observed. Except for the case of calcining at 400 °C, the rest of the calcination

https://doi.org/10.1021/acsomega.4c02423
ACS Omega 2024, 9, 40394−40410

temperatures resulted in similar conversions of CO, NO, and naphthalene. In other words, CO and naphthalene were fully converted in the 200−350 °C range, whereas a volcano-shaped conversion curve was observed for NO. The peaks for NO conversion were located at 278 °C (X_{NO} = 77%), 275 °C (X_{NO} = 64%), 276 °C (X_{NO} = 60%), and 268 °C (X_{NO} = 61%) for calcination temperatures of 450, 500, 550, and 600 °C, respectively. Interestingly, it is worth noting the full conversion of naphthalene over a large range of temperatures, which is usually reported to occur at higher temperatures with copper-based catalysts.[46] Figure 1F shows the presence of NO_2 at the exit of the reactor, which is an undesirable product due to its reactivity in the atmosphere to form acid rain(different volume gas cells and GHSVs were used to rule outgas-phase generation of NO_2). The presence of NO_2 was very small when the catalyst was calcined at 400 °C, especially in the range of 250−350 °C, where the activity of NO reduction was the highest. The generation of NO_2 was slightly higher when calcined at 450, 500, and 600 °C, and it was the smallest when the sample was calcined at 550 °C. Although not included in the figures, the selectivity to N_2 was almost 100% in all cases, except at 350 °C where it was 96%.It is worth noting that N_2O was not observed under any conditions in any of the catalysts.

As mentioned before, to simulate the natural accumulation of alkali and alkaline-earth metals, calcium was selected and added after the impregnation of copper. To understand the possible effect of copper being occluded by calcium, different loadings of calcium were studied on the *X*%Ca/Cu/$YCeO_2$−TiO_2 catalyst (*X* = 1.8, 2.6, 5.2, 13 wt %). The loading of copper was maintained at 2.6% for all samples, and the calcination temperature before the reaction was 450 °C to avoid possible sintering of the copper phase. The results of the reduction of NO with CO and naphthalene with oxygen are shown in Figure 2. Above 250 °C and despite the loading of Ca, there is not much change in the conversion of naphthalene and CO, reaching 100% conversion at higher temperatures. In the case of the 1.8%Ca/Cu/$YCeO_2$−TiO_2 catalyst, the NO conversion shows a volcano shape with a maximum of 77% at 278 °C. At higher Ca loadings, the volcano shape disappears, and the NO conversion curve gradually increases in each case, reaching NO conversions at 350 °C of 80, 90, and 87% for the catalysts with Ca loadings of 2.6, 5.2, and 13%, respectively. Additionally, below 200 °C, higher loadings of Ca favor the conversion of naphthalene, which remains close to 100% in all cases (except for the loading of 1.8% Ca). On the other hand, it seems to be an improvement in the conversion of CO with Ca, but it reverses with the loading of 13% Ca where the CO conversion is lower in the 100−200 °C range than the cases with 2.6% Ca and 5.2% Ca.

3.2. Nitrogen Adsorption−desorption. To verify possible textural effects on the activity of the catalysts, the N_2 isotherms were measured for the $YCeO_2$−TiO_2 support and for the Cu/$YCeO_2$−TiO_2 and Ca/Cu/$YCeO_2$−TiO_2catalysts. Figure 3A displays a maximum in the pore distribution centered at 5 nm for all samples. Then, the pore distribution decreases with larger pore sizes. On the other hand, the cumulative pore volume follows a similar trend for all samples, steadily increasing up to 20 nm, where a slight change in the slope is observed, and increasing again in the 20−30 nm range. Thus, the increase in the cumulative volume shown in Figure 3A indicates a gradual contribution of pores of larger size, which becomes accentuated for pores larger than 20 nm.

It is also observed that the addition of copper and calcium led to a decrease in the pore distribution slightly more visible at approximately 5 nm, possibly due to the occlusion of small pores after the impregnation of copper and calcium (Figure 3C). This effect is also noticed on the cumulative pore volume, which shows a slightly lower increase after each metal impregnation.

In the case of the N_2 isotherms, Figure 3B,3D, according to the IUPAC classification, the curves resemble a type-IV isotherms related to mesopores but with no plateau at high p/p_0, which belong to a pseudotype II or in between types II and IV with a H3 hysteresis type.[47] Additionally, the observed hysteresis might be related to compact agglomerates of uniform spherical particles.[48] Figure 3D also shows a lower adsorption volume when increasing the loading of calcium.

Table 1 shows that the calcined TiO_2 has an area of 105 m^2/g with a pore volume of 0.38 cm^3/g. After preparation and calcination of the $YCeO_2$−TiO_2 support, the area decreased to 76 m^2/g, possibly due to the partial blockage of the $YCeO_2$ phase. Nevertheless, this is a usable area for further copper and calcium impregnation steps. In fact, the Cu/$YCeO_2$−TiO_2 catalyst had an area of 62 m^2/g and a pore volume of 0.19 cm^3/g. After adding 1.8% calcium, a slight increase in the area was observed with 68 m^2/g and a similar effect with the pore volume with a value of 0.22 cm^3/g (only two decimals shown). These results show that although the addition of copper and calcium led to a slight blockage of pores, a significant area remained to allow the dispersion of the active phases. It should be noted that the samples were able to show thermal stability considering that after each impregnation, they were calcined at 500 °C. Upon increasing the loadings of Ca up to 2.6, 5.2, and 13%, the available area gradually decreases to 66, 59, and 54 m^2/g, respectively. Accordingly, the pore volume gradually decreases to values of 0.23, 0.21, and 0.18 with higher loadings of Ca. Notice that the latter pore volume value resembles that from the Cu/$YCeO_2$−TiO_2 catalyst, which indicates that the accumulation only slightly affects both the available area and pore volume of the samples. Table 1 also include the area and pore volume of the samples calcined at different temperatures before reaction. It is observed that the calcinations at 400 and 450 °C led to 44 m^2/g in both cases. These low values are likely due to either the presences of nitrates from the impregnation steps or lack of crystallization. Once the samples are calcined at 500 and 550 °C, the areas increased to 68 and 70 m^2/g, respectively. A slight decrease in the area (66 m^2/g)

Table 1. BET Area and Pore Volume Determined by N_2 Adsorption

sample	area $m^2\ g^{-1}$	pore volume $cm^3\ g^{-1}$
TiO_2	105	0.38
$YCeO_2$−TiO_2	76	0.21
Cu/$YCeO_2$−TiO_2	62	0.19
1.8Ca/Cu/$YCeO_2$−TiO_2	68	0.22
2.6Ca/Cu/$YCeO_2$−TiO_2	66	0.23
5.2Ca/Cu/$YCeO_2$−TiO_2	59	0.21
13Ca/Cu/$YCeO_2$−TiO_2	54	0.18
1.8Ca/Cu/$YCeO_2$−TiO_2calc. 400 °C	44	0.21
1.8Ca/Cu/$YCeO_2$−TiO_2calc. 450 °C	44	0.21
1.8Ca/Cu/$YCeO_2$−TiO_2calc. 500 °C	68	0.22
1.8Ca/Cu/$YCeO_2$−TiO_2calc. 550 °C	70	0.22
1.8Ca/Cu/$YCeO_2$−TiO_2calc. 600 °C	66	0.22

https://doi.org/10.1021/acsomega.4c02423
ACS Omega 2024, 9, 40394−40410

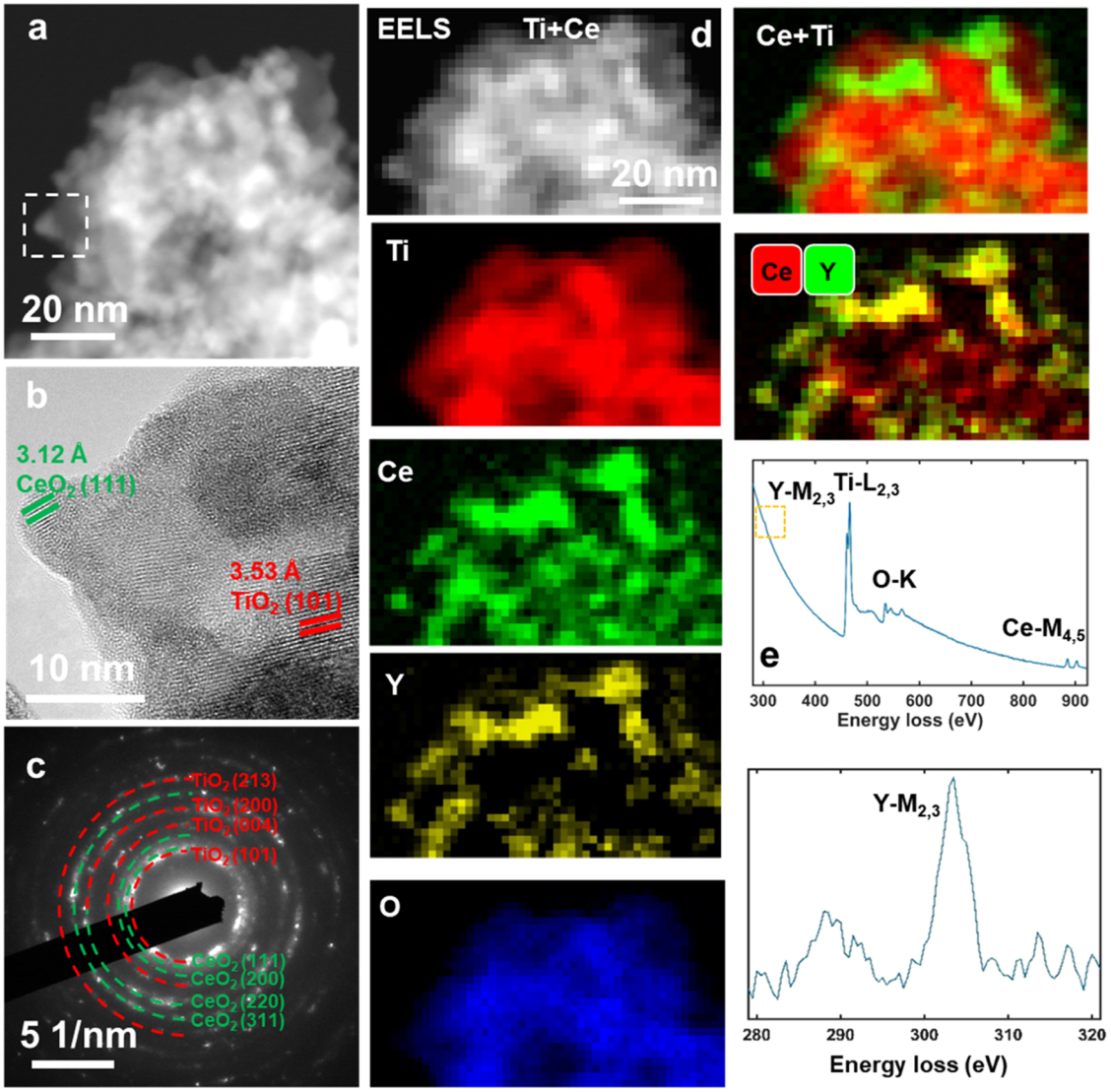

Figure 4. (a) HAADF, (b) HRTEM, (c) SAED, (d) EELS, and (e) EDX images of the calcined $YCeO_2-TiO_2$ support.

was observed when calcining at 600 °C. In all cases, the pore volume remained almost unchanged. It is clear that the effect of larger amounts of calcium on the surface area is more severe than the calcination temperature, which demonstrate the thermal stability of the catalysts.

3.3. Transmission Electron Microscopy. To identify the morphological structure of the catalyst, they were subjected to high-resolution transmission electron microscopy (HRTEM), and the results are shown in Figures 4 to 6. In the case of the $YCeO_2-TiO_2$ support, Figure 4a shows a high-angle annular dark field (HAADF) image of a mixture of CeO_2 (in bright contrast) and TiO_2 (in dark contrast) phases. The selected area in a dashed square Figure 4a shows as HRTEM in Figure 4b, where the $CeO_2(111)$ plane and TiO_2[101] plane are clearly observed. The selected area electron diffraction (SAED) image in Figure 4c only shows the contribution from different planes of the phases of CeO_2 and TiO_2 (the yttria phase was not detected). On the other hand, the electron energy loss spectroscopy (EELS) maps in Figure 4d show the element distribution where the TiO_2supportis clearly visible, whereas the Ce and Y phases are well distributed on the TiO_2 surface and show an intimate interaction between each phase. Notice that the energy dispersive X-ray (EDX) signal from the yttria phase, Figure 4e, is weak and barely appears in the EDX spectrum.

The same analysis on the $Cu/YCeO_2-TiO_2$ catalyst (2.6% Cu) is shown in Figure 5. Again, the HAADF image, Figure 5a, corresponds to a mixture of CeO_2 (in bright contrast) and TiO_2 (in dark contrast) nanoparticles. The HRTEM in the selected area, Figure 5b, shows the measured planes of the $CeO_2(111)$ plane and $TiO_2(004)$. Additionally, the SAED image, Figure 5c, shows the prevalence of different planes of CeO_2 and TiO_2. The EELS images from the selected dashed white line reveal that the distributions of yttria and ceria coincide and are both well distributed on the TiO_2 surface. The signal from the copper phase was too small to be detected, as exhibited by the EDX spectrum, Figure 5f, which was acquired from the large field of view shown in Figure 5e.

Next, the $Ca/Cu/YCeO_2-TiO_2$ catalyst (2.6% Cu, 1.8% Ca) is shown in Figure 6. As in the previous cases, the HAADF image, Figure 6a, gives a mixture of CeO_2 (in bright contrast) and TiO_2 (in dark contrast), which is consistent with the lattice fringes observed in Figure 6b from both phases. The SAED pattern, Figure 6c, indicates the crystalline character of

https://doi.org/10.1021/acsomega.4c02423
ACS Omega 2024, 9, 40394−40410

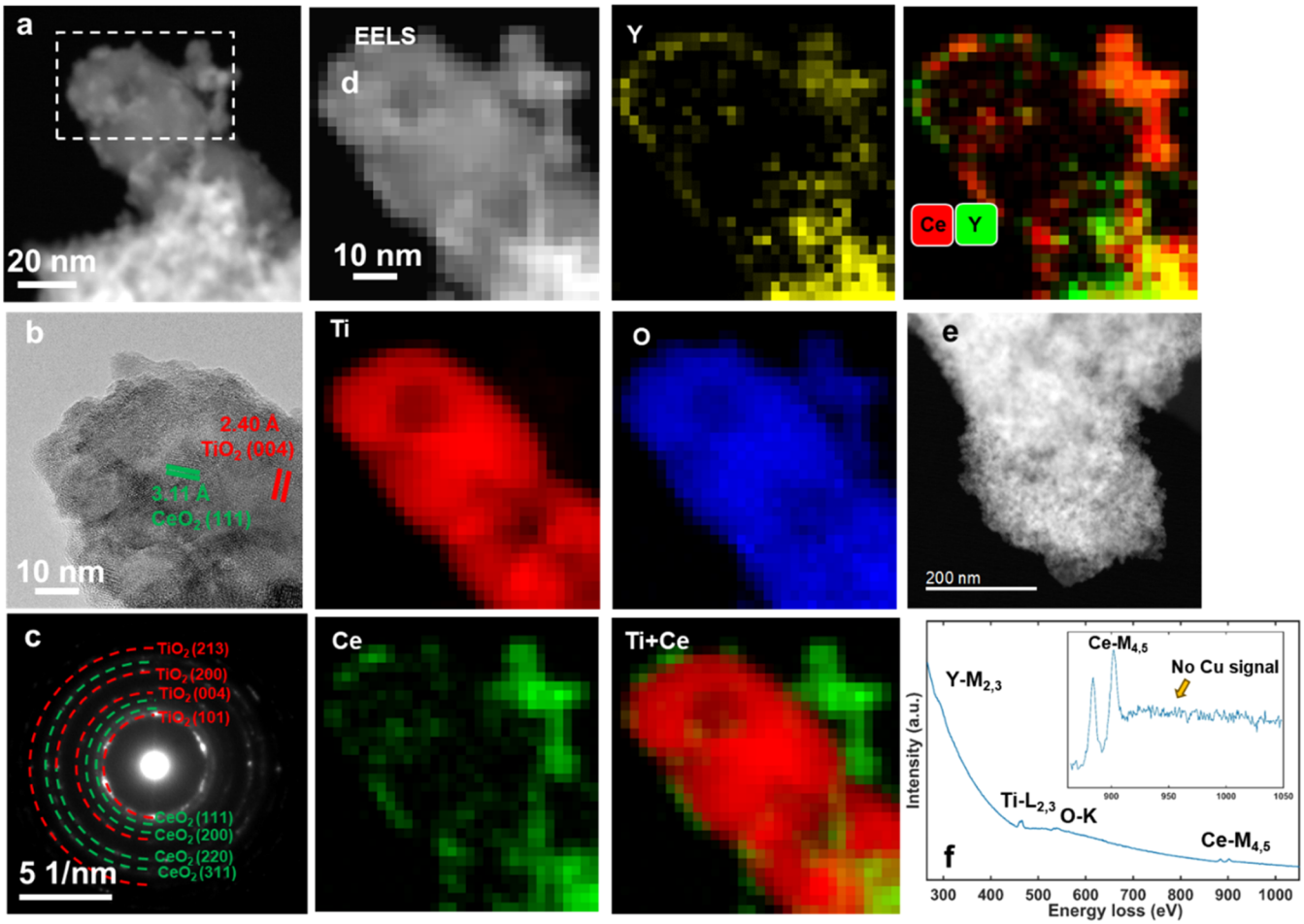

Figure 5. (a) HAADF, (b) HRTEM, (c) SAED, (d) EELS, and (e) EDX images of the calcined Cu/$YCeO_2$−TiO_2 catalyst.

both phases, CeO_2 and TiO_2. As with the previous samples, the overlap of the Ce and Y phases is evident, as both phases occupy similar locations. The calcium phase is well distributed throughout the surface. Again, the signal from the copper phase is too low to be detected in the selected large field of view.

3.4. H_2−Temperature-programmed Reduction (TPR). To study the reducibility of the samples, temperature-programmed reduction (TPR) experiments were performed. Figure 7 shows the results for the $YCeO_2$−TiO_2 support and the Cu/$YCeO_2$−TiO_2 and Ca/Cu/$YCeO_2$−TiO_2 catalysts.

In Figure 7A, the TPR corresponding to the support shows a broad reduction peak in the range of 520−630 °C, which is associated with the reduction of labile and low-coordinated oxygen atoms on the CeO_2 surface.[49−51] After adding copper, a set of reduction peaks are observed (see peak decomposition in Figure 7A, top curve, a Gaussian fit was used in all cases), which are assigned to the reduction of copper with different degrees of agglomeration. Highly dispersed small copper particles are the first to be reduced (217 °C), followed by larger particles that have not yet formed crystallites (230 °C) and finally the reduction of small dispersed crystallites of copper (241 °C).[52−54] Again, a broad but smaller reduction shoulder is observed at high temperature and centered at approximately 530 °C, corresponding to the reduction of oxygen atoms from the support.

In the case of the Ca/Cu/$YCeO_2$−TiO_2 catalyst, as shown in Figure 7A, a similar reduction profile is obtained as with the copper-only sample discussed before. However, all the reduction peaks are displaced to higher temperatures on the Ca/Cu/$YCeO_2$−TiO_2 catalyst, and the reduction profile is slightly smaller than that of the Cu/$YCeO_2$−TiO_2 catalyst. The shift in the reduction temperatures to higher values is associated with the presence of calcium, which is an electropositive atom that interacts with neighboring oxygen atoms in contact with copper, which in turn is more difficult to reduce. In other words, oxygen atoms are harder to remove (reduced) in the presence of calcium, and therefore, slightly higher reduction temperatures are needed. The smaller overall reduction on the Ca/Cu/$YCeO_2$−TiO_2 catalyst might be due to either the occlusion of copper atoms after impregnating calcium or that the Cu−O−Ca interaction is strong enough to avoid the reduction of such copper sites.

The effect of higher loadings of Ca on the reduction of copper is shown in Figure 7B. For different loadings of Ca, the reduction profiles are similar in the temperature range of 50−450 °C. However, these profiles show certain differences in the deconvoluted peaks and in the size of the whole reduction area between 150 and 300 °C. With respect to the decomposition of peaks, the lower temperature peak (linked to highly dispersed small copper particles) appears at a higher temperature on the 1.8Ca/Cu/$YCeO_2$−TiO_2 catalyst than on the other catalysts with higher loadings of calcium, where the position of this peak remains constant. Additionally, the lower temperature reduction peak is the highest on the 2.6Ca/Cu/$YCeO_2$−TiO_2 catalyst. If the total reduction area is considered

https://doi.org/10.1021/acsomega.4c02423
ACS Omega 2024, 9, 40394−40410

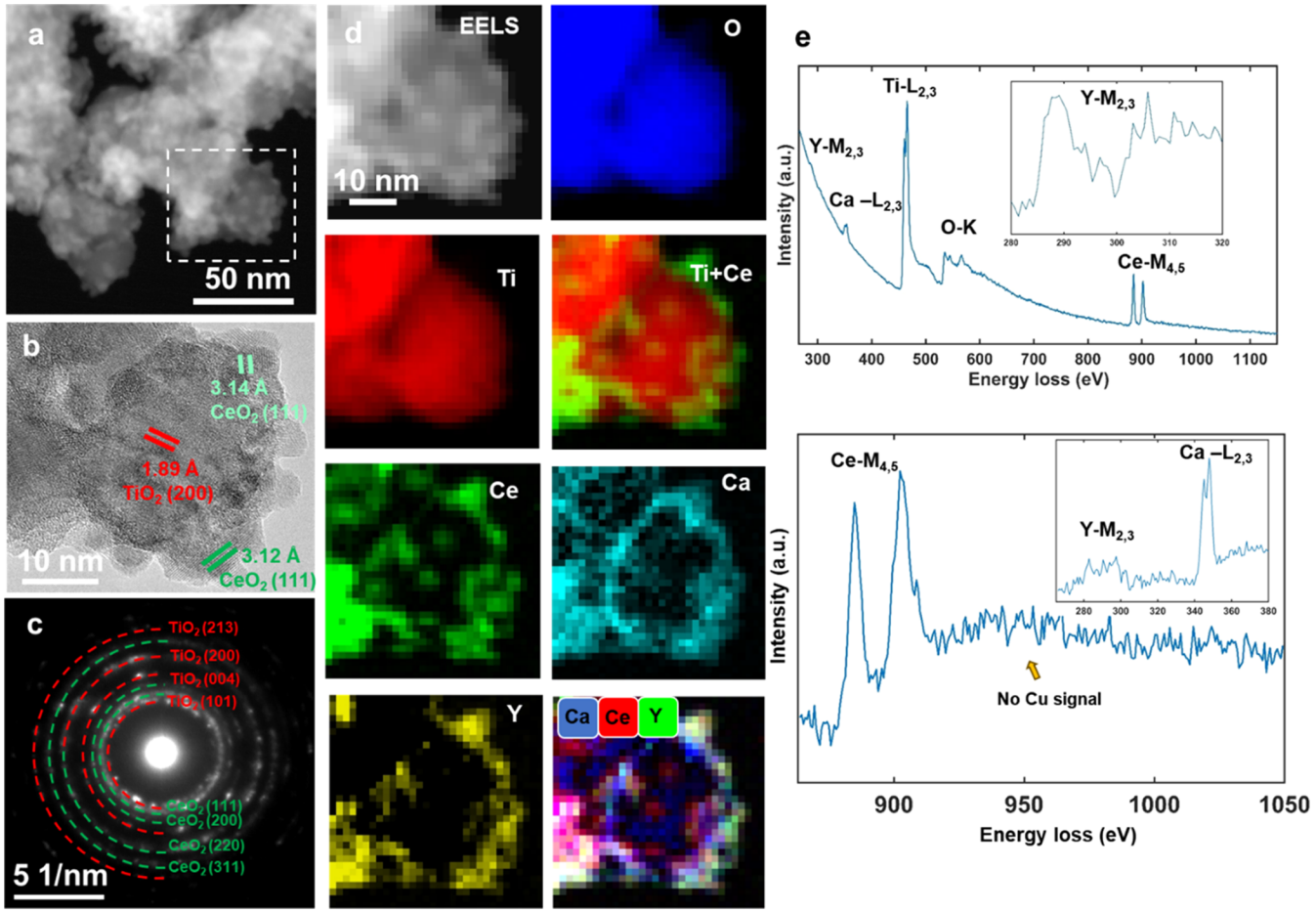

Figure 6. (a) HAADF, (b) HRTEM, (c) SAED, (d) EELS, and (e) EDX images of the calcined Ca/Cu/$YCeO_2$−TiO_2 catalyst.

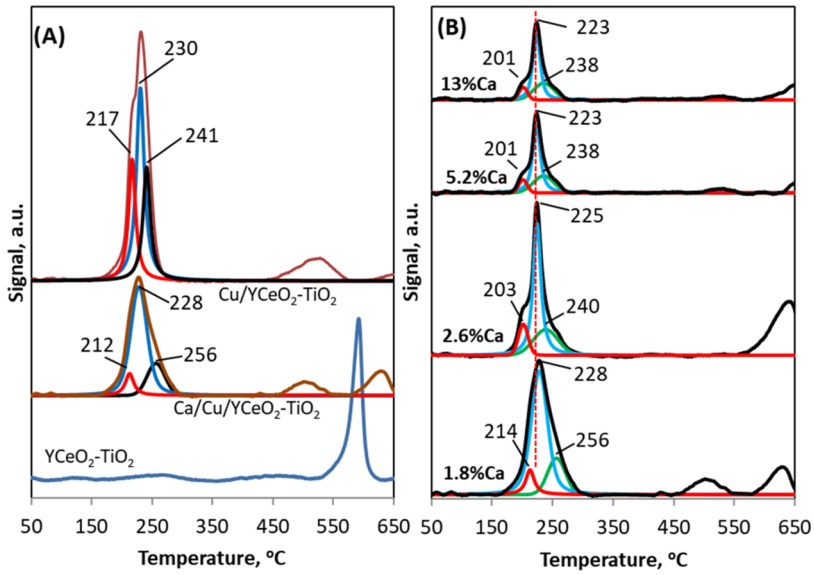

Figure 7. H_2−Temperature-programmed reduction (from top to bottom) of (A) Cu/$YCeO_2$−TiO_2, Ca/Cu/$YCeO_2$−TiO_2, and the support $YCeO_2$−TiO_2. Peaks are numbered in centigrades; (B) Ca/Cu/$YCeO_2$−TiO_2 with constant loading of Cu (2.6%) and varying loadings of Ca: 1.8, 2.6, 5.2, and 13%. Gaussian fit was used in all cases with no restriction on the peaks positions or widths.

between 150 and 300 °C, the 1.8Ca/Cu/$YCeO_2$−TiO_2 and 2.6Ca/Cu/$YCeO_2$−TiO_2 catalysts have a similar consumption of hydrogen. When increasing the loading of Ca, it is observed that the reduction area decreases for the 5.2Ca/Cu/$YCeO_2$−TiO_2 and 13Ca/Cu/$YCeO_2$−TiO_2 catalysts. Notwithstanding this decrease in the reduction profile, these catalysts remain active. In other words, the oxidation properties of the catalysts are not greatly affected by increasing amounts of Ca.

3.5. Diffuse Reflectance Infrared Experiments (DRIFTS). Operando DRIFTS analysis was performed on the

https://doi.org/10.1021/acsomega.4c02423
ACS Omega 2024, 9, 40394−40410

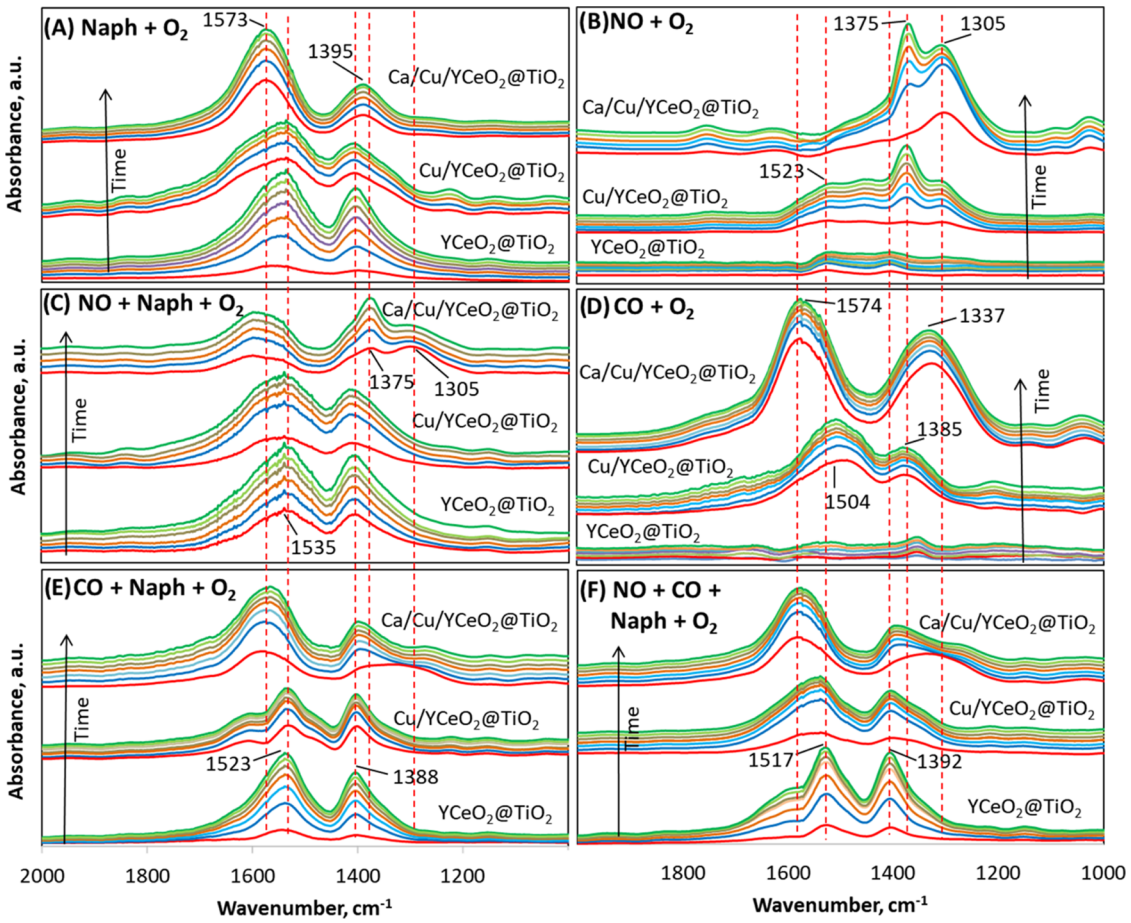

Figure 8. DRIFT spectra of the $Ca/Cu/YCeO_2$-TiO_2 and $Cu/YCeO_2$−TiO_2 catalysts and the $YCeO_2$−TiO_2 support under the reactions of (A) naphthalene oxidation (500 ppm naphthalene and 10% O_2), (B) NO oxidation (500 ppm of NO and 10% O_2), (C) reduction of NO with naphthalene (500 ppm of NO, 500 ppm naphthalene, and 10% O_2), (D) oxidation of CO (1% CO and 10% oxygen), (E) oxidation of naphthalene and CO (500 ppm naphthalene, 1% CO, and 10% oxygen), and (F) reduction of NO with CO and naphthalene(500 ppm of NO, 500 ppm naphthalene, 1% CO, and 10% oxygen). Helium was used as balance in all cases. All samples were diluted in KBr (catalyst/KBr = 1:9). Reaction temperature: 350 °C, duration of the reaction: 1 h.

$Ca/Cu/YCeO_2$−TiO_2 and $Cu/YCeO_2$−TiO_2 catalysts and on the $YCeO_2$−TiO_2 support (1.8% Ca and 2.6% Cu were considered). Apart from the selective reduction of NO with CO and naphthalene, separate reactions were also studied to relate adsorbed species and particular reaction paths. Figure 8 shows the spectra from the naphthalene oxidation reaction, NO oxidation, reduction of NO with naphthalene, oxidation of CO, oxidation of naphthalene and CO, and the reduction of NO with CO and naphthalene. It is observed that different infrared absorption bands develop with time and although overlapping of signals is unavoidable, some features can be identified: carbonates or nitrate/nitrite species around 1523−1517 and 1535 cm^{-1},[55] hyponitrites(NO^-, $N_2O_2^{2-}$) on highly basic sites at 1305 and 1375 cm^{-1},[56] bidentate nitrates at 1305 cm^{-1},[57,58] monodentate carbonates at 1337 and 1523 cm^{-1},[59] bidentate carbonates at 1573 cm^{-1}[60] (some reports relate these species to being adsorbed on basic sites of ceria[56,61−64]), formate species interacting with hydroxyls present on the surface around 1520 cm^{-1} and hydrogen carbonates species at 1395 cm^{-1}.[65] Figure 8A shows that bidentate and hydrogen carbonates are the main species under naphthalene oxidation, which is similar to the case of CO and naphthalene oxidation (Figure 8C), CO oxidation (Figure 8D), and during the oxidation of both CO and naphthalene (Figure 8E). In fact, similar species appear under the reduction of NO with CO and naphthalene (Figure 8F). It can be noticed that in all cases when CO or naphthalene are involved, bidentate carbonates experiment a blue-shift in the sample containing calcium. The addition of calcium induces a blue-shift in the infrared absorption of carbonates, which could be associated with an electron density transfer from the carbonyl group to the metal which lead to an increase in the C−O bond strength.[66] The latter explains the increase in reduction temperature shown in the TPR results in the samples containing calcium, which is due to a higher interaction of the carbonyl bond with the adsorption site. During CO oxidation, the main peaks at 1574 and 1337 cm^{-1} are associated with carbonates adsorbed on nonreduced CeO_2 sites with a $\Delta\nu_{as\text{-}s}$ of 237 cm^{-1}.[67]

In the case of NO oxidation, nitrites/nitrates are the main observed species (Figure 8B), especially on the sample containing calcium. It is likely that calcium contributes to a more electropositive surface facilitating the adsorption of nitrites/nitrates. Such species are also observed during the reduction of NO with naphthalene (Figure 8C) along with carbonates species, which shows that nitrates and carbonates coexist during this reaction. In the case of the reduction of NO with CO and naphthalene (Figure 8F), carbonates are mainly observed, whereas nitrate species barely appear in the spectra,

https://doi.org/10.1021/acsomega.4c02423
ACS Omega 2024, 9, 40394−40410

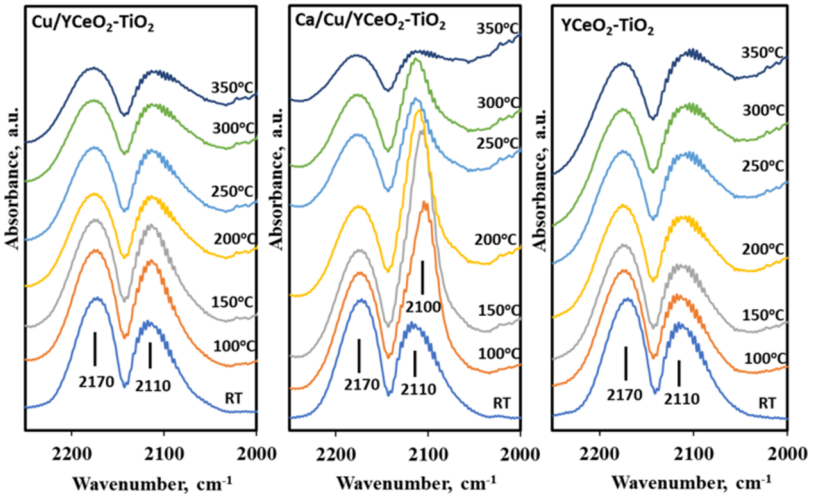

Figure 9. DRIFT spectra of the selective reduction of NO with CO and naphthalene on the 1.8Ca/Cu/$YCeO_2$−TiO_2 and Cu/$YCeO_2$−TiO_2 catalysts and the $YCeO_2$−TiO_2 support. All samples were diluted in KBr (catalyst/KBr = 1:9). Reaction conditions: 500 ppm of NO, 1% CO, 10% O_2, He balance.

which points to a dominance of carbonate during this reaction. Nevertheless, it should be noted that only 500 ppm of NO are used against 1% CO during the reduction of NO with CO and naphthalene and the predominance of carbonate species is expected.

Also, a distinctive feature appeared in the 2250−2000 cm^{-1} range, which corresponds to the range where a gas-phase carbon monoxide doublet appeared (2170 and 2110 cm^{-1}). Figure 9 shows that for the Ca/Cu/$YCeO_2$−TiO_2 catalyst, a feature appears at 2100^{-1}, which has been ascribed to CO adsorbed on Cu^+.[65,68−70] This peak is clearly visible from 100 to 300 °C. In the case of the Cu/$YCeO_2$−TiO_2 catalyst and for the $YCeO_2$−TiO_2 support, such a signal is not clearly developed, showing only the absorbance peaks corresponding to gas-phase carbon monoxide. The shifting of the baseline at high wavenumbers was due to thermal effects upon heating the samples, and no correction was applied to avoid altering the intensity of the signals previously mentioned.

3.6. X-ray Diffraction (XRD). In order to analyze the crystallinity of the samples, X-ray diffraction patterns were recorded for the Ca/Cu/$YCeO_2$−TiO_2 and Cu/$YCeO_2$−TiO_2 catalysts and for the $YCeO_2$−TiO_2 support. Figure 10 shows the characteristics diffraction signals from the tetragonal TiO_2 at 25.5, 38, and 49°, which correspond to the,[101] (112), and (200) planes of anatase (JCPDS #21−1272). In the case of the diffraction signals from CeO_2 and Y_2O_3 (yttria was used as stabilizer of the surface area of CeO_2), they all overlap ((111), (200), (220), and (311) planes of the cubic fluorite structure of CeO_2, JCPDS #810792, and the (222), (400), (440), and (541) planes of body centered cubic Y_2O_3, JCPDS #88−1040). Diffraction signals from copper or calcium were not detected possibly due to too small aggregates of these phases to be able to contribute to diffraction, which is consistent with the HRTEM analysis.

3.7. Raman Spectroscopy. The crystalline character of the sample under reaction conditions is shown in Figure 11using Raman spectroscopy in the range of 50−1000 cm^{-1}. The observed spectrum is typical of anatase TiO_2 with bands at 647 cm^{-1} (E_g), 511 cm^{-1} (A_{1g}), 399 cm^{-1} (B_{1g}), 198 cm^{-1} (E_g), and 144 cm^{-1} (E_g), which is consistent with the XRD results. On the other hand, the signal from the F_{2g} symmetry of

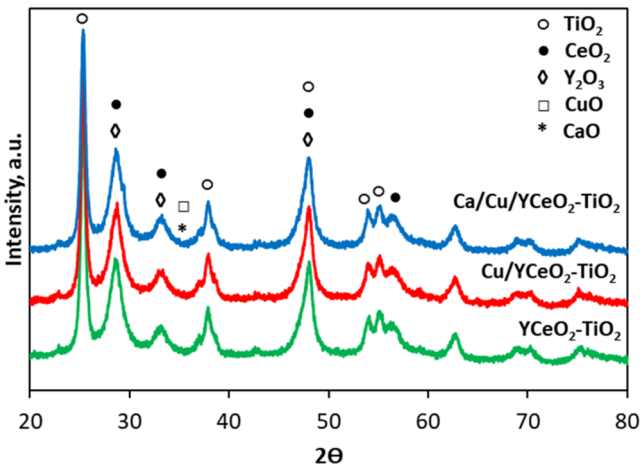

Figure 10. X-ray diffraction from the Ca/Cu/$YCeO_2$−TiO_2 and Cu/$YCeO_2$−TiO_2 catalysts and the $YCeO_2$−TiO_2 support. Each curve is correspondingly labeled.

CeO_2 is barely observed at 460 cm^{-1}, possibly due to occlusion from the TiO_2 phase and because of the more defective structure of ceria. To support the latter point, the inset in Figure 11A shows high-resolution spectra in the 700−1000 cm^{-1} region, where a peak at ca. 820 cm^{-1} indicates the presence of adsorbed oxygen species on the two-electron defects of CeO_2.[71]

Figure 11B shows a similar Raman shift for the samples with different loadings of Ca, except for the CeO_2 signal at 460 cm^{-1}, which disappears at loadings of 5.2% Ca and 13% Ca, possibly due to the occlusion of copper by larger amounts of calcium. Nevertheless, the inset in Figure 11B reveals that the signal from oxygen adsorbed on CeO_2 defects remains almost unchanged.

3.8. X-ray Photoelectron Spectroscopy (XPS). The chemical and electronic speciation of the catalyst was studied by performing XPS analysis on the 1.8Ca/Cu/$YCeO_2$−TiO_2 and Cu/$YCeO_2$−TiO_2 samples (2.6% Cu in both cases). Figure 12A,12B show the Ce 3d XPS high-resolution spectra, which are formed by a composition of components associated with the oxidation states of Ce(III) and Ce(IV). In the case of

https://doi.org/10.1021/acsomega.4c02423
ACS Omega 2024, 9, 40394−40410

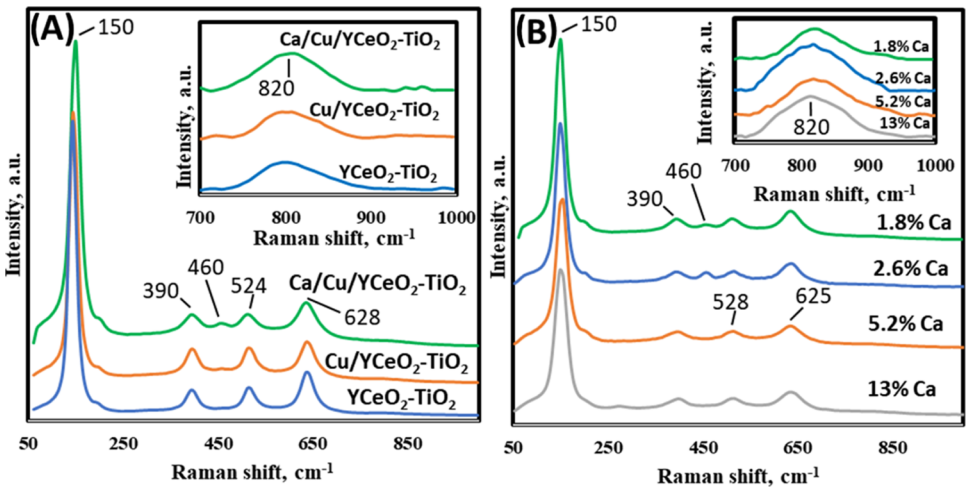

Figure 11. (A) Operando Raman results during the reduction of NO with CO and naphthalene in the presence of oxygen on the Ca/Cu/$YCeO_2$−TiO_2 and Cu/$YCeO_2$−TiO_2 catalysts and the $YCeO_2$−TiO_2 support and (B) with varying loading of Ca on the Ca/Cu/$YCeO_2$−TiO_2 catalyst. All measurements were done with a laser of 532 nm with a diameter beam of ∼1.2 nm and a grating of 600 g/mm.

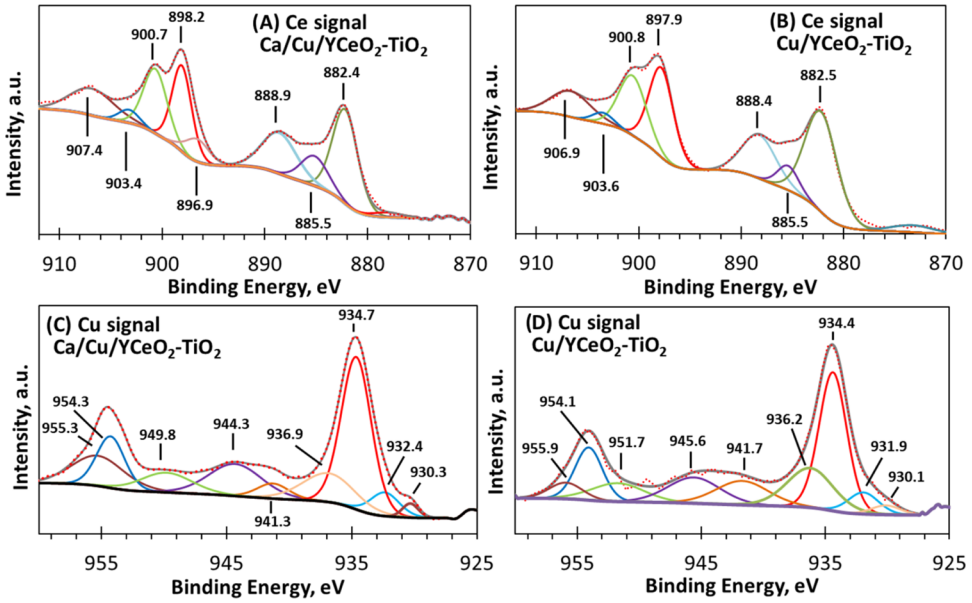

Figure 12. XPS high-resolution spectra of Ce 3d (A, B) and Cu 2p (C, D) for the Cu/$YCeO_2$−TiO_2 and Ca/Cu/$YCeO_2$−TiO_2 catalysts, respectively.

the Ca/Cu/$YCeO_2$−TiO_2 catalysts (Figure 12A), the Ce $3d_{5/2}$ and Ce $3d_{3/2}$ signals are observed at 882.4 and 900.7 eV, respectively, which coincides with the expected doublet ascribed to the spin−orbit splitting of Ce 3d (ΔE_{sl} = 18.3 eV).[72] In the case of the Cu/$YCeO_2$−TiO_2 catalysts, Figure 12B, the position of this doublet was very similar as well (882.5 eV, 900.8 eV, ΔE_{sl} = 18.3 eV).[72] The peaks at 882.4, 888.9, and 898.2 eV are assigned to Ce(IV) $3d_{5/2}$ for the Ca/Cu/$YCeO_2$−TiO_2 catalysts, whereas the same peaks are located at 882.5, 888.4, and 897.9 eV for the Cu/$YCeO_2$−TiO_2 catalysts. The peaks assigned to Ce(IV) $3d_{3/2}$ were located at 900.7 and 907.4 eV for the Ca/Cu/$YCeO_2$−TiO_2 catalysts (900.8 and 906.9 eV for the Cu/$YCeO_2$−TiO_2 catalysts).[73,74] Notice that the peak decomposition gives two peaks at 885.5 eV and ∼903.5, which are associated with the presence of Ce^{3+}.[75]

The Cu 2p XPS spectra of the doublets of Cu $2p_{1/2}$ and Cu $2p_{3/2}$ are shown in Figure 12C−D. The main signals of Cu $2p_{3/2}$ were located at 934.6 and 934.4 eV, whereas the signals from Cu $2p_{1/2}$ were at 954.7 and 954.1 eV for the Ca/Cu/$YCeO_2$−TiO_2 and Cu/$YCeO_2$−TiO_2 catalysts, respectively (spin energy separation of ∼20 eV). The latter together with adjacent peaks at 941.3−941.7 and 944.3−945.6 eV confirm the presence of Cu^{2+} in both samples.[76,77] In both cases, the satellite structure of Cu 2p is typical of Cu^{2+}, but the relative intensity of the main Cu $2p_{3/2}$ peak to the satellite located at 944.3 and 945.6 eV in both samples gives a ratio of ∼0.37. This low value suggests that some of the copper might be present as Cu^{1+}. In fact, the appearance of a signal at 932.4 eV (Figure 12C) and 931.9 (Figure 12D) associated with Cu^{1+} indicates the presence of this oxidation state of copper.[78,79] The small contribution at 930.1−930.3 eV has also been assigned to Cu^{1+}.[80] The peak observed at 936.9−936.2 was assigned to $Cu(OH)_2$.[81] The XPS from Ca 2p, Ti 2p, Y 3d, and O 1s, and O are provided in Figure S1 in the Supporting Information.

To monitor the changes on the surface of the catalysts with different loadings of Ca, XPS analyses were performed on all

https://doi.org/10.1021/acsomega.4c02423
ACS Omega 2024, 9, 40394−40410

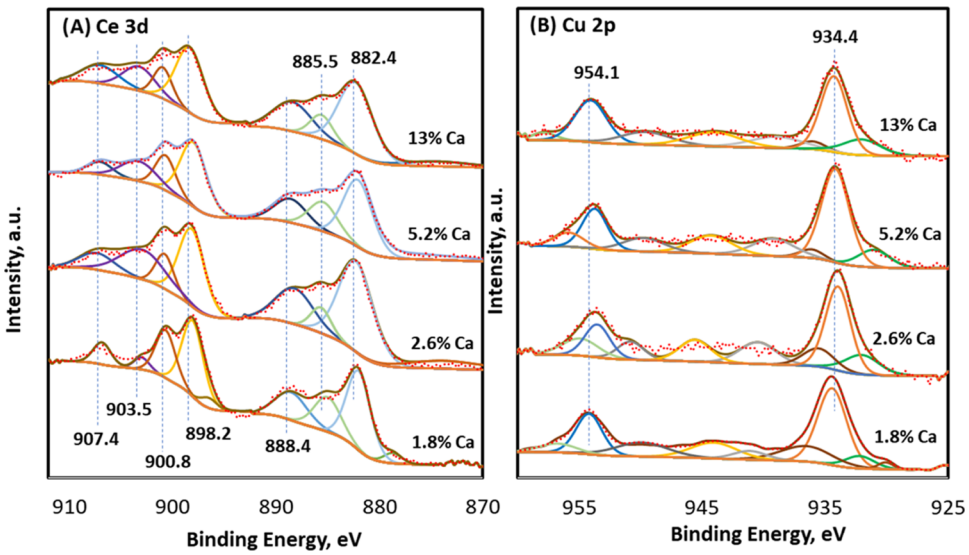

Figure 13. XPS high-resolution spectra of Ca/Cu/$YCeO_2$−TiO_2 catalysts with varying loadings of calcium. (A) Ce 3d, (B) Cu 2p.

samples. The results are shown in Figure 13. The signal from Ce 3d, Figure 13A, shows that the spectra are similar under different loadings of calcium. In fact, all curves show the presence of Ce^{3+} at approximately 885.5 and 903.5 eV. In a similar fashion, despite the expected higher coverage of calcium, the signal from Cu 2p is clearly observed in all samples (Figure 13B). In fact, the decomposition of each spectrum shows a signal at approximately 931.9 eV associated with Cu^{1+}. Figure S2 in the Supporting Information shows the signals from C 1s, O 1s, and Ca 2p with different loadings of Ca.

In terms of a quantitative analysis of the results, the complexity of the samples did not facilitate a proper fitting of all signals since the intensity and the multiple overlapping of signals from different phases became an important hurdle. For this reason, we were cautious to restrict the above analysis to a qualitative level.

4. DISCUSSION

The activity results show that the catalysts are resistant to the accumulation of calcium and to thermal treatments, and they can fully eliminate CO and naphthalene. Of course, these reducers are partially utilized in the reduction of NO, and interesting conversions of NO are also achieved at 350 °C. What is remarkable is that no occlusion of the active phases occurs when larger amounts of calcium are added to the catalyst. In fact, it should be noted that the decrease in the available surface area is not proportional to the increase in Ca in the catalyst; that is, based on the 1.8%Ca, an increase of 1.5 times (2.6%Ca), 2.9 times (5.2%Ca), and 7.2 times (13%Ca) did not lead to a proportional decrease in the area (66, 59, and 54 m^2/g) with respect to the 68 m^2/g that the 1.8Ca/Cu/$YCeO_2$−TiO_2 catalyst had. The HRTEM analyses show a homogeneous distribution of species with the Ce and Y phases observed in intimate contact, which is consistent with the preparation of the support where yttrium was added to grant thermal stability to the CeO_2 phase; thus, it is expected that both phases, Y−Ce, are in close contact. Thus, the stability of the surface area might be because larger amounts of calcium are well distributed on the catalyst surface, with the available active sites not being occluded at any time, as demonstrated by the activity of the catalysts. In this sense, it is worth mentioning that all the results show a stable TiO_2 support, which is able to provide a proper surface area to disperse the CeO_2 phase.

The appearance of Ce^{3+} and Cu^{+} during the characterization of the catalysts suggests the presence of the redox pairs Cu^{2+}/Cu^{+} and Ce^{4+}/Ce^{3+} ($Ce^{3+} + Cu^{2+} \leftrightarrow Ce^{4+} + Cu^{+}$) in these materials. On the other hand, electropositive Ca has the potential to alter the electronic environment or such pairs and affect the reduction of not only copper but also ceria.[31] The latter is reflected in the activity of the catalysts since the catalytic performance of the CuO_x−CeO_2 catalyst has been ascribed to the redox potential of copper species interacting with the CeO_2 support.[82−84] Such interaction between copper and ceria is expected, although the role of other surface species, such as yttrium oxide and titanium oxide, might have similar interactions with CuO_x in the sense of sharing oxygen species or defect sites, which affect the reducibility of copper in the presence of calcium. As shown by the Raman results, such defects are present in all the studied samples. This low coordination character of ceria together with the high dispersion of small aggregates of copper can lead to the presence of a copper-ceria interface where the unsaturation of the latter influences the degree of interaction of copper sites with surrounding oxygen atoms. Moreover, if the presence of calcium is also considered, the interaction of such oxygen species with copper differs from copper−oxygen when calcium is not present in the sense that calcium exerts an extra electronic force upon these shared oxygen atoms. The latter is reflected in a shift of the reduction temperature to higher values (see TPR results, Figure 7). In other words, copper is more difficult to reduce due to the extra force provided by the electropositive Ca. Thus, even under highly oxidizing conditions, semireduced species of copper and cerium can coexist. In fact, the existence of reduced species of copper and cerium has been reported in calcined catalysts.[85,86] Such species might be present on the calcium-free samples but are less noticeable due to lower concentrations of such species. Therefore, it is likely that the existence of defect sites on the ceria surface can result in the formation of Cu−O_x−Ce structures where copper is in high interaction with the ceria support.[87] In this sense, the electronic modification by the

https://doi.org/10.1021/acsomega.4c02423
ACS Omega 2024, 9, 40394−40410

presence of calcium might provide the conditions to facilitate the redox cycle between Cu^{2+}/Cu^{+} and Ce^{4+}/Ce^{3+} on these sites. The appearance of CO adsorbed on Cu^{1+} during the reduction of NO with CO and naphthalene (DRIFTS in Figure 9) and in XPS (together with Ce^{3+}) are consistent with the idea of the formation of sites having a Cu−O_x−Ce structure. Moreover, the presence of oxygen species adsorbed on ceria defects, as shown by the Raman results (Figure 11), might be related to this Cu−O_x−Ce interface. It has been proposed that extra oxygen vacancies are generated by the incorporation of Cu^{2+} cations in the CeO_2 fluorite lattice as a compensation mechanism of the valence mismatch between Cu^{2+} and Ce^{4+}.[88−91] The absence of copper from the HRTEM images suggests that this metal is highly dispersed on the surface, which agrees with the TPR results, and therefore thoroughly dispersed on the support. It is highly likely that the fraction of copper interacting with the ceria phase participates in a redox exchange. This high dispersion agrees with the observed activity of the catalysts, which is barely affected by higher amounts of calcium, which shows that the active Cu−O_x−Ce pairs are small enough to not be hindered (at least by a large amount) by the aggregates of calcium that are formed on the surface and that are observed in the HRTEM images. The persistence of CeO_2 defects with larger amounts of calcium observed with Raman is consistent with the idea of such small Cu−O_x−Ce sites that are not affected by the addition of calcium forming large aggregates. In any case, calcium might play a positive role during the reaction, not only altering the electronic environment of the Cu−O_x−Ce site but also suppressing the formation of coke by increasing the basicity of the catalyst, as reported in other works,[31,92−100] and preventing the copper phase from sintering.[101,102] The latter seems to be an important effect based on the degree of aggregation of the calcium phase observed on HRTEM, which acts as a barrier preventing copper from forming large aggregates and reinforcing the Cu−O_x−Ce interaction (more energy is needed for the reduction of copper). Again, as mentioned above, the TiO_2 support serves as a scaffold to disperse the CeO_2 phase and, in turn, the copper phase, which results in a proper dispersion of Cu−O_x−Ce sites. The inclusion of yttrium serves not only as a thermal stabilizer of the CeO_2 phase but also to favor the presence of oxygen-unsaturated ceria sites where Ce^{3+} species are more likely to exist. It has been proposed that the hybridization of Ce^{3+} with TiO_2 takes place through the interaction of Ce 4f and the O 2p band of TiO_2,[103,104] which in turn avoids sintering of the CeO_2 phase. The latter favors the conditions to have a high dispersion of Cu−O_x−Ce sites. In this regard, it should be noted that an attempt to report turnover frequencies was avoided due to the arguable significance of measuring copper dispersion by regular techniques, because the actual active site seems to be much more complex in the present catalytic system. Thus, more work needs to be done to converge to a reliable titration technique able to represent such complex systems.

Although it was not the purpose of this study to elucidate the reaction mechanism of the reduction of NO with CO and naphthalene in the presence of oxygen, it is worth mentioning that the presence of some surface species seems to be significant in this reaction. The following discussion, although speculative, has a contributory purpose in ideas that emerge from looking at the mechanism of the reaction, and it could be useful to those exploring this problem. As mentioned above, the combination of Cu^{1+} and Ce^{3+} has been reported to be very active as a redox pair ($Ce^{3+} + Cu^{2+} \leftrightarrow Ce^{4+} + Cu^{+}$), and as the reaction takes place in oxidative conditions, it is expected that both species are readily oxidized to Cu^{2+} and Ce^{4+}. From the viewpoint of NO, the reduction takes place by first being oxidized to NO_2, which is readily adsorbed as nitrates and nitrites,[29] but mainly as hyponitrites (Figure 8B). Such species are then reduced to N_2 by CO and naphthalene. Apart from the formation of adsorbed carbonates (Figure 8), no other species of intermediates are observed; in particular, no byproducts of naphthalene oxidation were observed in any of the experiments carried out. It is likely that the pathways of naphthalene oxidation are fast enough to not be able to observe any other species during the reaction. On the other hand, the active sites for NO oxidation to NO_2, naphthalene oxidation, CO oxidation, and the reduction of NO with either naphthalene, CO, or both, seem to be not exclusive for each reaction. All mentioned reactions involve an oxygen exchange, which would justify the existence of a site of the Cu−O_x−Ce type, where O_x corresponds to a labile oxygen occupying the vacancy in a shared Cu−Ce site. Martinez-Arias et al.,[68] investigating CO oxidation on a $CuO/CeZrO_4$ catalyst, proposed the interaction of CO and oxygen by oxygen adsorbed in vacancies (VÖ) located in the interface between ceria and copper

$$(Ce^{+4}-O^{-2}-Cu^{+2}) + CO \rightarrow (Ce^{+3}-V\ddot{O}-Cu^{+1}) + CO_2 \quad (3)$$

A similar scenario might occur with the oxidation of naphthalene. However, given the higher complexity of this molecule, a more convoluted pathway is needed for the oxidation of naphthalene. Nevertheless, as the reaction shown above, a simplified step can be proposed

$$n(Ce^{+4}-O^{-2}-Cu^{+2}) + C_{10}H_8 \rightarrow n(Ce^{+3}-V\ddot{O}-Cu^{+1}) + 10CO_2 + 4H_2O \quad (4)$$

The "*n*" prefix is included to emphasize that more than one Cu−O_x−Ce site may participate in the oxidation of one molecule of naphthalene. The scenario described by the previous reactions assumes that both CO and naphthalene are fully oxidized to gaseous products, but in the presence of NO, it is necessary to consider that CO and the naphthalene intermediates (Cu^{+1}−CO) and (Cu^{+1}−C_xH_y) are also reducing for example contiguous adsorbed nitrates ($M^{+}NO_3^{-}$) into molecular nitrogen, where M represents a calcium site contiguous to the active sites where nitrates are preferentially being adsorbed. In this case, the presence of Cu^{+} might play an important role, such as

$$n(M^{+}NO_3^{-}) + (Cu^{+1}-C_xH_y) \rightarrow nMO + nCuO + N_2 + CO_2 + H_2O \quad (5)$$

$$n(M^{+}NO_3^{-}) + (Cu^{+1}-CO) \rightarrow nMO + nCuO + N_2 + CO_2 \quad (6)$$

where MO represents the oxidized phase of Ca. Both the adsorbed CO and the adsorbed naphthalene intermediates act as reducers of the adsorbed nitrate species, changing copper back to Cu^{2+}. The occurrence of the reaction in oxidizing conditions favors the presence of atomic oxygen to replenish the oxygen vacancies. Of course, that the actual mechanism

https://doi.org/10.1021/acsomega.4c02423
ACS Omega 2024, 9, 40394−40410

could be much more complicated than the description above, but at least it set a basis of discussion on the possible pathways that these reactions could take place. What is clear is that the oxidation of CO and naphthalene occurs in parallel with the reduction of NO as shown by the infrared results, where part of the CO and naphthalene are used as reducers of the adsorbed nitrogen species. Experiments are underway to clarify the actual mechanism of this reaction.

5. CONCLUSIONS

The results presented here show a highly active copper catalyst in the reduction of NO with CO and naphthalene in the presence of oxygen. The strategy of dispersing a stabilized ceria phase on TiO_2 leads to a proper $YCeO_2$−TiO_2 support, that can disperse the copper phase in a manner that shows high activity over a wide range of temperatures.

The gradual accumulation of alkaline and alkaline earth metals on a working catalyst was simulated here by the impregnation of different amounts of calcium on a Cu/$YCeO_2$−TiO_2 catalyst. The result shows that the copper phase resists the gradual accumulation of calcium on the Ca/Cu/$YCeO_2$−TiO_2 catalyst, and a high activity on the reduction of NO was maintained. Moreover, total conversion of CO and naphthalene was observed on all catalysts containing different loadings of Ca over a wide range of temperatures. The results suggest that the calcium aggregates act as barriers for the copper, preventing the sintering of this phase and favoring the high dispersion of copper. The latter, together with the large dispersion of ceria, benefits the interaction between copper and the ceria support.

In summary, these promising results show that the proper preparation of a support is a determining step in providing a high dispersion of the active copper phase, which is resistant to poisoning or accumulation of alkaline and alkaline earth metals generated during combustion.

■ ASSOCIATED CONTENT

Supporting Information

The Supporting Information is available free of charge at https://pubs.acs.org/doi/10.1021/acsomega.4c02423.

Additional XPS spectra of Ca, Ti, Y, C, and O (PDF)

■ AUTHOR INFORMATION

Corresponding Author

Sichem Guerrero Ruz − *Universidad de los Andes, Chile, Facultad de Ingeniería y Ciencias Aplicadas, 12455 Las Condes, Chile;* orcid.org/0000-0003-0281-3390; Phone: +56 2 2618 1327; Email: sguerrero@miuandes.cl

Authors

Josefina Herrera − *Universidad de los Andes, Chile, Facultad de Ingeniería y Ciencias Aplicadas, 12455 Las Condes, Chile*

Gonzalo Aguila − *Departamento de Ciencias de la Ingenieria, Facultad de Ingenieria, Universidad Andres Bello, Santiago 7500971, Chile;* orcid.org/0000-0003-3441-4175

Ye Zhu − *Department of Applied Physics, Hong Kong Polytechnic University, Kowloon 999077 Hong Kong, China*

ZhiHang Xu − *Department of Applied Physics, Hong Kong Polytechnic University, Kowloon 999077 Hong Kong, China*

Complete contact information is available at: https://pubs.acs.org/10.1021/acsomega.4c02423

Notes

The authors declare no competing financial interest.

■ ACKNOWLEDGMENTS

The Chilean National Science and Technology Research Fund, FONDECYT REGULAR project N° 1220582, is gratefully acknowledged for funding this work.

■ REFERENCES

(1) World Energy Outlook 2022 2022 https://www.iea.org/reports/world-energy-outlook-2022/outlook-for-energy-demand.

(2) World Health Organization 2023 https://www.who.int/data/gho/data/themes/air-pollution.

(3) Smith, K. R.; Uma, R.; Kishore, V. V. N.; Zhang, J.; Joshi, V.; Khalil, M. A. K. Greenhouse Implications of Household Stoves: An Analysis for India. *Annu. Rev. Energy Environ.* **2000**, *25* (1), 741−763.

(4) Abdel-Shafy, H. I.; Mansour, M. S. M. A review on polycyclic aromatic hydrocarbons: Source, environmental impact, effect on human health and remediation. *Egypt. J. Pet.* **2016**, *25* (1), 107−123.

(5) Arbex, M. A.; Cançado, J. E. D.; Pereira, L. A. A.; Braga, A. L. F.; do Nascimento Saldiva, P. H. Queima de biomassa e efeitos sobre a saúde. *J. Bras Pneumol.* **2004**, *30* (2), 158−175.

(6) Zhang, J. J.; Smith, K. R. Household Air Pollution from Coal and Biomass Fuels in China: Measurements, Health Impacts, and Interventions. *Environ. Health Perspect.* **2007**, *115* (6), 848−855.

(7) Wei, L.; Yu, C.; Yang, K.; Fan, Q.; Ji, H. Recent advances in VOCs and CO removal via photothermal synergistic catalysis. *Chin. J. Catal.* **2021**, *42* (7), 1078−1095.

(8) Li, Y. J.; Armor, J. N. Selective Catalytic Reduction of NO with Methane on Gallium Catalysts. *J. Catal.* **1994**, *145* (1), 1−9.

(9) Kikuchi, E.; Yogo, K. Selective catalytic reduction of nitrogen monoxide by methane on zeolite catalysts in an oxygen-rich atmosphere. *Catal. Today.* **1994**, *22* (1), 73−86.

(10) Burch, R.; Millington, P. J. Role of propene in the selective reduction of nitrogen monoxide in copper-exchanged zeolites. *Appl. Catal., B* **1993**, *2* (1), 101−116.

(11) Quincoces, C. E.; Kikot, A.; Basaldella, E. I.; González, M. G. Effect of Hydrothermal Treatment on Cu-ZSM-5 Catalyst in the Selective Reduction of NO. *Ind. Eng. Chem. Res.* **1999**, *38* (11), 4236−4240.

(12) Lionta, G. D.; Christoforou, S. C.; Efthimiadis, E. A.; Vasalos, I. A. Selective Catalytic Reduction of NO with Hydrocarbons: Experimental and Simulation Results. *Ind. Eng. Chem. Res.* **1996**, *35* (8), 2508−2515.

(13) Gunes, H.; Yıldız, D. Ş.; Özener, B.; Hisar, G.; Rommel, S.; Aindow, M.; et al. Preparation of Pt/Al_2O_3 and $PtPd/Al_2O_3$ catalysts by supercritical deposition and their performance for oxidation of nitric oxide and propene. *Catal. Today* **2022**, *388*−*389*, 70−78.

(14) Yuan, M.; Deng, W.; Dong, S.; Li, Q.; Zhao, B.; Su, Y. Montmorillonite based porous clay heterostructures modified with Fe as catalysts for selective catalytic reduction of NO with propylene. *Chem. Eng. J.* **2018**, *353*, 839−848.

(15) Xu, G.; Ma, J.; He, G.; Yu, Y.; He, H. An alumina-supported silver catalyst with high water tolerance for H_2 assisted C_3H_6-SCR of NOx. *Appl. Catal., B* **2017**, *207*, 60−71.

(16) Zhou, H.; Ge, M.; Zhao, H.; Wu, S.; Li, M.; Su, Y. Selective Catalytic Reduction of Nitric Oxide with Propylene over Fe/Beta Catalysts Under Lean-Burn Conditions. *Catalysts* **2019**, *9* (2), No. 205.

(17) Zhou, H.; Ge, M.y.; Zhao, H.s.; Wu, S.g.; Ye, B.c.; Su, Y.x. Selective catalytic reduction of nitric oxide with propylene in excess oxygen over Fe-Mn/Beta catalysts. *J. Fuel Chem. Technol.* **2019**, *47*, 751−761.

(18) Burch, R.; Scire, S. Selective catalytic reduction of nitric oxide with ethane and methane on some metal exchanged ZSM-5 zeolites. *Appl. Catal., B* **1994**, *3* (4), 295−318.

(19) Long, R. Q.; Yang, R. T. Selective Catalytic Reduction of Nitric Oxide with Ethylene on Copper Ion-Exchanged Al−MCM-41 Catalyst. *Ind. Eng. Chem. Res.* **1999**, *38* (3), 873−878.
(20) Zhou, H.; Ge, M.; Wu, S.; Ye, B.; Su, Y. Iron based monolithic catalysts supported on Al_2O_3, SiO_2, and TiO_2: A comparison for NO reduction with propane. *Fuel* **2018**, *220*, 330−338.
(21) Moreno-González, M.; Palomares, A. E.; Chiesa, M.; Boronat, M.; Giamello, E.; Blasco, T. Evidence of a Cu^{2+}−Alkane Interaction in Cu-Zeolite Catalysts Crucial for the Selective Catalytic Reduction of NOx with Hydrocarbons. *ACS Catal.* **2017**, *7* (5), 3501−3509.
(22) Kalamaras, C. M.; Olympiou, G. G.; Pârvulescu, V. I.; Cojocaru, B.; Efstathiou, A. M. Selective catalytic reduction of NO by H_2/C_3H_6 over $Pt/Ce_{1-x}Zr_xO_{2-\delta}$: The synergy effect studied by transient techniques. *Appl. Catal., B* **2017**, *206*, 308−318.
(23) Gu, H.; Chun, K. M.; Song, S. The effects of hydrogen on the efficiency of NOx reduction via hydrocarbon-selective catalytic reduction (HC-SCR) at low temperature using various reductants. *Int. J. Hydrogen Energy.* **2015**, *40* (30), 9602−9610.
(24) Stere, C. E.; Adress, W.; Burch, R.; Chansai, S.; Goguet, A.; Graham, W. G.; et al. Ambient Temperature Hydrocarbon Selective Catalytic Reduction of NO_x Using Atmospheric Pressure Nonthermal Plasma Activation of a Ag/Al_2O_3 Catalyst. *ACS Catal.* **2014**, *4* (2), 666−673.
(25) Roberts, K. L.; Amiridis, M. D. Kinetic Investigation of the Selective Catalytic Reduction of Nitric Oxide by Propylene over Pt/Al_2O_3. *Ind. Eng. Chem. Res.* **1997**, *36* (9), 3528−3532.
(26) Hamill, C.; Burch, R.; Goguet, A.; Rooney, D.; Driss, H.; Petrov, L.; Daous, M. Evaluation and mechanistic investigation of a AuPd alloy catalyst for the hydrocarbon selective catalytic reduction (HC-SCR) of NO_x. *Appl. Catal., B* **2014**, *147*, 864−870.
(27) Onda, A.; Suzuki, Y.; Kajiyoshi, K.; Yanagisawa, K. Catalytic Performance of Autoclave Liners in the Wet Oxidation of Naphthalene. *Ind. Eng. Chem. Res.* **2006**, *45* (7), 2194−2198.
(28) Schiefer, H. B.; Irvine, D. G.; Buzik, S. C. *Understanding Toxicology: Chemicals, Their Benefits and Risks*; Informa Healthcare, 1997.
(29) Venegas, F.; López, N.; Sánchez-Calderón, L.; Aguila, G.; Araya, P.; Guo, X.; et al. The transient reduction of NO with CO and naphthalene in the presence of oxygen using a core−shell $SmCeO_2$@ TiO_2-supported copper catalyst. *Catal. Sci. Technol.* **2019**, *9* (13), 3408−3415.
(30) Morales, C.; López, N.; Aguila, G.; Araya, P.; Scott, F.; Vergara-Fernández, A.; Guerrero, S. Simultaneous use of CO and naphthalene for the reduction of NO on potassium promoted copper catalyst supported on Ce/TiO_2-SiO_2 and in the presence of oxygen. *Mater. Chem. Phys.* **2019**, *222*, 294−299.
(31) Sánchez, L.; Aguila, G.; Araya, P.; Quijada, S.; Guerrero, S. A highly active $Ca/Cu/YCeO_2$−TiO_2 catalyst for the transient reduction of NO with CO and naphthalene under oxidizing conditions. *RSC Adv.* **2021**, *11* (63), 39896−39906.
(32) Konsolakis, M. The role of Copper−Ceria interactions in catalysis science: Recent theoretical and experimental advances. *Appl. Catal., B* **2016**, *198*, 49−66.
(33) Wang, H.; Dang, X.; Huang, Y.; Wang, W.; Yan, D.; Yu, X.; et al. Research progress of Cu-based and Ce-based catalysts for the selective catalytic reduction of NO with CO. *Surf. Interfaces* **2024**, *48*, No. 104310.
(34) Zhou, Y.; Chen, A.; Ning, J.; Shen, W. Electronic and geometric structure of the copper-ceria interface on Cu/CeO2 catalysts. *Chin. J. Catal.* **2020**, *41* (6), 928−937.
(35) Senanayake, S. D.; Stacchiola, D.; Rodriguez, J. A. Unique Properties of Ceria Nanoparticles Supported on Metals: Novel Inverse Ceria/Copper Catalysts for CO Oxidation and the Water-Gas Shift Reaction. *Acc. Chem. Res.* **2013**, *46* (8), 1702−1711.
(36) Stacchiola, D. J. Tuning the Properties of Copper-Based Catalysts Based on Molecular in Situ Studies of Model Systems. *Acc. Chem. Res.* **2015**, *48* (7), 2151−2158.
(37) Águila, G.; Gracia, F.; Araya, P. CuO and CeO_2 catalysts supported on Al_2O_3, ZrO_2, and SiO_2 in the oxidation of CO at low temperature. *Appl. Catal., A* **2008**, *343* (1), 16−24.
(38) Aguila, G.; Guerrero, S.; Baeza, P.; Araya, P. Study of the influence of the Cu/Ce loading ratio in the formation of highly active species on ZrO_2 supported copper-ceria catalysts. *Mater. Chem. Phys.* **2019**, *223*, 666−675.
(39) Xu, Y.; Gao, L.; Ding, Z. Synthesis and Oxygen Storage Capacities of Yttrium-Doped CeO_2 with a Cubic Fluorite Structure. *Materials* **2022**, *15*, No. 8971, DOI: 10.3390/ma15248971.
(40) Akbari-Fakhrabadi, A.; Saravanan, R.; Jamshidijam, M.; Mangalaraja, R. V.; Gracia, M. A. Preparation of nanosized yttrium doped CeO2 catalyst used for photocatalytic application. *J. Saudi Chem. Soc.* **2015**, *19* (5), 505−510.
(41) Kurapova, O. Y.; Shugurov, S. M.; Vasil'eva, E. A.; Savelev, D. A.; Konakov, V. G.; Lopatin, S. I. Thermal prehistory, structure and high-temperature thermodynamic properties of Y_2O_3-CeO_2 and Y_2O_3-ZrO_2-CeO_2 solid solutions. *Ceram. Int.* **2021**, *47* (8), 11072−11079.
(42) Zhu, Y.; Liu, X.; Shi, W.; Li, J.; Ye, C.; Fang, R.; et al. Effect of yttrium and manganese addition on catalytic soot combustion activity and anti-high-temperature stability of CeO_2 catalyst. *J. Rare Earths* **2024**, *42* (2), 334−344.
(43) Xu, B.; Zhang, Q.; Yuan, S.; Zhang, M.; Ohno, T. Synthesis and photocatalytic performance of yttrium-doped CeO2 with a porous broom-like hierarchical structure. *Appl. Catal., B* **2016**, *183*, 361−370.
(44) Guerrero, S.; Guzmán, I.; Aguila, G.; Chornik, B.; Araya, P. Study of $Na/Cu/TiO_2$ catalysts for the storage and reduction of NO. *Appl. Catal., B* **2012**, *123*−*124*, 282−295.
(45) Guerrero, S.; Águila, G.; Araya, P. Lean NO adsorption on copper catalysts supported on ceria and promoted with sodium. *Catal. Commun.* **2012**, *28*, 183−90.
(46) Aranda, A.; Agouram, S.; López, J. M.; Mastral, A. M.; Sellick, D. R.; Solsona, B.; et al. Oxygen defects: The key parameter controlling the activity and selectivity of mesoporous copper-doped ceria for the total oxidation of naphthalene. *Appl. Catal., B* **2012**, *127*, 77−88.
(47) Saber, O.; Gobara, H. M. Optimization of silica content in alumina-silica nanocomposites to achieve high catalytic dehydrogenation activity of supported Pt catalyst. *Egypt. J. Pet.* **2014**, *23* (4), 445−454.
(48) Sing, K. S. W. Reporting physisorption data for gas/solid systems with special reference to the determination of surface area and porosity (Recommendations 1984). *Pure Appl. Chem.* **1985**, *57* (4), 603−619.
(49) Papavasiliou, J.; Rawski, M.; Vakros, J.; Avgouropoulos, G. A Novel Post-Synthesis Modification of CuO-CeO_2 Catalysts: Effect on Their Activity for Selective CO Oxidation. *ChemCatChem* **2018**, *10* (9), 2096−2106.
(50) Sun, S.; Mao, D.; Yu, J. Enhanced CO oxidation activity of CuO/CeO_2 catalyst prepared by surfactant-assisted impregnation method. *J. Rare Earths* **2015**, *33* (12), 1268−1274.
(51) Papadopoulos, C.; Kappis, K.; Papavasiliou, J.; Vakros, J.; Kuśmierz, M.; Gac, W.; et al. Copper-promoted ceria catalysts for CO oxidation reaction. *Catal. Today* **2020**, *355*, 647−653.
(52) Li, C.; Yang, Y.; Ren, W.; Wang, J.; Zhu, T.; Xu, W. Effect of Ce Doping on Catalytic Performance of Cu/TiO_2 for CO Oxidation. *Catal. Lett.* **2020**, *150* (7), 2045−2055.
(53) Dong, F.; Meng, Y.; Han, W.; Zhao, H.; Tang, Z. Morphology effects on surface chemical properties and lattice defects of Cu/CeO_2 catalysts applied for low-temperature CO oxidation. *Sci. Rep.* **2019**, *9* (1), No. 12056.
(54) Yao, X.; Xiong, Y.; Sun, J.; Gao, F.; Deng, Y.; Tang, C.; Dong, L. Influence of MnO_2 modification methods on the catalytic performance of CuO/CeO_2 for NO reduction by CO. *J. Rare Earths* **2014**, *32* (2), 131−138.
(55) Socrates, G. *Infrared and Raman Characteristic Group Frequencies: Tables and Charts*; Wiley, 2004.

https://doi.org/10.1021/acsomega.4c02423
ACS Omega 2024, 9, 40394−40410

(56) Sedlmair, C.; Seshan, K.; Jentys, A.; Lercher, J. A. Elementary steps of NOx adsorption and surface reaction on a commercial storage−reduction catalyst. *J. Catal.* **2003**, *214* (2), 308−316.
(57) Zhang, L.; Pierce, J.; Leung, V. L.; Wang, D.; Epling, W. S. Characterization of Ceria's Interaction with NOx and NH_3. *J. Phys. Chem. C* **2013**, *117* (16), 8282−8289.
(58) Mihaylov, M. Y.; Zdravkova, V. R.; Ivanova, E. Z.; Aleksandrov, H. A.; Petkov, P. S.; Vayssilov, G. N.; Hadjiivanov, K. Infrared spectra of surface nitrates: Revision of the current opinions based on the case study of ceria. *J. Catal.* **2021**, *394*, 245−258.
(59) Ho, K. Y.; Yeung, K. L. Properties of TiO_2 support and the performance of Au/TiO_2 Catalyst for CO oxidation reaction. *Gold Bull.* **2007**, *40* (1), 15−30.
(60) Hester, R. E.; Grossman, W. E. L. Vibrational Analysis of Bidentate Nitrate and Carbonate Complexes. *Inorg. Chem.* **1966**, *5* (8), 1308−1312.
(61) Szanyi, J.; Kwak, J. H.; Kim, D. H.; Burton, S. D.; Peden, C. H. F. NO_2 Adsorption on BaO/Al_2O_3: The Nature of Nitrate Species. *J. Phys. Chem. B* **2005**, *109* (1), 27−29.
(62) Martínez-Arias, A.; Hungría, A. B.; Iglesias-Juez, A.; Fernández-García, M.; Anderson, J. A.; Conesa, J. C.; et al. Redox and catalytic properties of CuO/CeO_2 under CO+O_2+NO: Promoting effect of NO on CO oxidation. *Catal. Today* **2012**, *180* (1), 81−87.
(63) Yang, Z.; Woo, T. K.; Hermansson, K. Adsorption of NO on unreduced and reduced CeO_2 surfaces: A plane-wave DFT study. *Surf. Sci.* **2006**, *600* (22), 4953−4960.
(64) Niwa, M.; Furukawa, Y.; Murakami, Y. Adsorption of nitric oxide on cerium oxide. *J. Colloid Interface Sci.* **1982**, *86* (1), 260−265.
(65) Baidya, T.; Bera, P. Investigation of support effect on CO adsorption and CO + O_2 reaction over $Ce_{1-x-y}M_xCu_yO_{2-\delta}$ (M = Zr, Hf and Th) catalysts by in situ DRIFTS. *Catal. Struct. React.* **2015**, *1* (3), 110−119.
(66) Manzoli, M. Boosting the Characterization of Heterogeneous Catalysts for H_2O_2 Direct Synthesis by Infrared Spectroscopy. *Catalysts* **2019**, *9* (1), No. 30.
(67) Hemmingsson, F.; Schaefer, A.; Skoglundh, M.; Carlsson, P. A. CO_2 Methanation over Rh/CeO_2 Studied with Infrared Modulation Excitation Spectroscopy and Phase Sensitive Detection. *Catalysts* **2020**, *10* (6), No. 601.
(68) Martínez-Arias, A.; Fernández-García, M.; Hungría, A. B.; Iglesias-Juez, A.; Gálvez, O.; Anderson, J. A.; et al. Redox interplay at copper oxide-(Ce,Zr)O_x interfaces: influence of the presence of NO on the catalytic activity for CO oxidation over CuO/$CeZrO_4$. *J. Catal.* **2003**, *214* (2), 261−272.
(69) Hornés, A.; Bera, P.; Cámara, A. L.; Gamarra, D.; Munuera, G.; Martínez-Arias, A. CO-TPR-DRIFTS-MS in situ study of CuO/$Ce_{1-x}Tb_xO_{2-y}$ (x = 0, 0.2 and 0.5) catalysts: Support effects on redox properties and CO oxidation catalysis. *J. Catal.* **2009**, *268* (2), 367−375.
(70) Bera, P.; Cámara, A. L.; Hornés, A.; Martínez-Arias, A. Comparative in Situ DRIFTS-MS Study of ^{12}CO- and ^{13}CO-TPR on CuO/CeO_2 Catalyst. *J. Phys. Chem. C* **2009**, *113* (24), 10689−10695.
(71) Pushkarev, V. V.; Kovalchuk, V. I.; d'Itri, J. L. Probing Defect Sites on the CeO_2 Surface with Dioxygen. *J. Phys. Chem. B* **2004**, *108* (17), 5341−5348.
(72) Maslakov, K. I.; Teterin, Y. A.; Ryzhkov, M. V.; Popel, A. J.; Teterin, A. Y.; Ivanov, K. E.; et al. The electronic structure and the nature of the chemical bond in CeO_2. *Phys. Chem. Chem. Phys.* **2018**, *20* (23), 16167−16175.
(73) Guo, S.; Sun, W.; Yang, W.; Xu, Z.; Li, Q.; Shang, J. K. Synthesis of Mn_3O_4/CeO_2 Hybrid Nanotubes and Their Spontaneous Formation of a Paper-like, Free-Standing Membrane for the Removal of Arsenite from Water. *ACS Appl. Mater. Interfaces.* **2015**, *7* (47), 26291−26300.
(74) Qi, L.; Yu, Q.; Dai, Y.; Tang, C.; Liu, L.; Zhang, H.; et al. Influence of cerium precursors on the structure and reducibility of mesoporous CuO-CeO_2 catalysts for CO oxidation. *Appl. Catal., B* **2012**, *119*−*120*, 308−320.
(75) Zeng, S.; Bai, X.; Wang, X.; Yu, W.; Liu, Y. Valence State of Active Copper in CuO_x/CeO_2 Catalysts for CO Oxidation. *J. Rare Earths* **2006**, *24* (2), 177−181.
(76) Ai, Z.; Zhang, L.; Lee, S.; Ho, W. Interfacial Hydrothermal Synthesis of Cu@Cu_2O Core−Shell Microspheres with Enhanced Visible-Light-Driven Photocatalytic Activity. *J. Phys. Chem. C* **2009**, *113* (49), 20896−20902.
(77) Chen, F.; Zhao, X.; Liu, H.; Qu, J. Reaction of $Cu(CN)_3^{2-}$ with H_2O_2 in water under alkaline conditions: Cyanide oxidation, Cu^+/Cu^{2+} catalysis and H_2O_2 decomposition. *Appl. Catal., B* **2014**, *158*−*159*, 85−90.
(78) Swadźba-Kwaśny, M.; Chancelier, L.; Ng, S.; Manyar, H. G.; Hardacre, C.; Nockemann, P. Facile in situ synthesis of nanofluids based on ionic liquids and copper oxide clusters and nanoparticles. *Dalton Trans.* **2012**, *41* (1), 219−227.
(79) Xu, D.; Cheng, F.; Lu, Q.; Dai, P. Microwave Enhanced Catalytic Degradation of Methyl Orange in Aqueous Solution over CuO/CeO_2 Catalyst in the Absence and Presence of H_2O_2. *Ind. Eng. Chem. Res.* **2014**, *53* (7), 2625−2632.
(80) Monte, M.; Munuera, G.; Costa, D.; Conesa, J. C.; Martínez-Arias, A. Near-ambient XPS characterization of interfacial copper species in ceria-supported copper catalysts. *Phys. Chem. Chem. Phys.* **2015**, *17* (44), 29995−30004.
(81) Dan, Z.; Yang, Y.; Qin, F.; Wang, H.; Chang, H. Facile Fabrication of Cu_2O Nanobelts in Ethanol on Nanoporous Cu and their Photodegradation of Methyl Orange. *Materials* **2018**, *11* (3), No. 446.
(82) Bera, P.; Hegde, M. S.; Mitra, S.; Sampath, S. Promoting effect of CeO in a Cu/CeO catalyst: lowering of redox potentials of Cu species in the CeO matrix. *Chem. Commun.* **2001**, No. 10, 927−928.
(83) Yang, B.; Deng, W.; Guo, L.; Ishihara, T. Copper-ceria solid solution with improved catalytic activity for hydrogenation of CO_2 to CH_3OH. *Chin. J. Catal.* **2020**, *41* (9), 1348−1359.
(84) Shi, C.; Xu, L.; Zhu, A.; Zhang, Y.; Au, C. T. Copper Oxide Clusters Stabilized by Ceria for CO, C_3H_6, and NO Abatement. *Chin. J. Catal.* **2012**, *33* (9), 1455−1462.
(85) Avgouropoulos, G.; Ioannides, T.; Matralis, H. Influence of the preparation method on the performance of CuO−CeO_2 catalysts for the selective oxidation of CO. *Appl. Catal., B* **2005**, *56* (1), 87−93.
(86) Martínez-Arias, A.; Hungría, A. B.; Munuera, G.; Gamarra, D. Preferential oxidation of CO in rich H_2 over CuO/CeO_2: Details of selectivity and deactivation under the reactant stream. *Appl. Catal., B* **2006**, *65* (3), 207−216.
(87) Wang, F.; Yu, Z.; Zhai, S.; Li, Y.; Xu, Y.; Ye, Y.; et al. CuO decorated vacancy-rich CeO_2 nanopencils for highly efficient catalytic NO reduction by CO at low temperature. *Environ. Sci. Pollut Res.* **2023**, *30* (11), 31895−31904.
(88) Yang, F.; Wei, J.; Liu, W.; Guo, J.; Yang, Y. Copper doped ceria nanospheres: surface defects promoted catalytic activity and a versatile approach. *J. Mater. Chem. A* **2014**, *2* (16), 5662−5667.
(89) Zhou, Y.; Chen, A.; Ning, J.; Shen, W. Electronic and geometric structure of the copper-ceria interface on Cu/CeO_2 catalysts. *Chin. J. Catal.* **2020**, *41* (6), 928−937.
(90) Dinh, M. T. N.; Nguyen, C. C.; Phan, N. H. T.; Phuc, H. D. N.; Van Le, Q.; Kim, S. Y.; Nguyen-Dinh, L. Tailoring Oxygen Vacancies and Active Surface Oxygen Species in Copper-Doped MnO_2 Catalysts for Total Catalytic Oxidation of VOCs. *Ind. Eng. Chem. Res.* **2023**, *62* (18), 6908−6919.
(91) Zhang, S.; Jiang, B.; Tong, M.; Yang, Y.; Liao, Z.; Huang, Z.; et al. Efficient Cu/CeO_2 for Ketonization of Carboxylic Acids with Synergistic Interactions. *Ind. Eng. Chem. Res.* **2023**, *62*, 20667−20676.
(92) Yang, G.; Yu, H.; Huang, X.; Peng, F.; Wang, H. Effect of calcium dopant on catalysis of Ir/La_2O_3 for hydrogen production by oxidative steam reforming of glycerol. *Appl. Catal., B* **2012**, *127*, 89−98.
(93) Bando, K. K.; Soga, K.; Kunimori, K.; Arakawa, H. Effect of Li additive on CO_2 hydrogenation reactivity of zeolite supported Rh catalysts. *Appl. Catal., A* **1998**, *175* (1), 67−81.

https://doi.org/10.1021/acsomega.4c02423
ACS Omega 2024, 9, 40394−40410

(94) Miao, Q.; Xiong, G.; Sheng, S.; Guo, X. Control of the directions of oxidative transformation of methane over nickel-based catalysts by acid-base properties. *React. Kinet. Catal. Lett.* **1997**, *62* (2), 363−370.
(95) Chang, J. S.; Park, S. E.; Yoo, J. W.; Park, J. N. Catalytic Behavior of Supported KNiCa Catalyst and Mechanistic Consideration for Carbon Dioxide Reforming of Methane. *J. Catal.* **2000**, *195* (1), 1−11.
(96) Osaki, T.; Mori, T. Role of Potassium in Carbon-Free CO_2 Reforming of Methane on K-Promoted Ni/Al_2O_3 Catalysts. *J. Catal.* **2001**, *204* (1), 89−97.
(97) Juan-Juan, J.; Román-Martínez, M. C.; Illán-Gómez, M. J. Catalytic activity and characterization of Ni/Al_2O_3 and NiK/Al_2O_3 catalysts for CO_2 methane reforming. *Appl. Catal., A* **2004**, *264* (2), 169−174.
(98) Choong, C. K. S.; Huang, L.; Zhong, Z.; Lin, J.; Hong, L.; Chen, L. Effect of calcium addition on catalytic ethanol steam reforming of Ni/Al_2O_3: II. Acidity/basicity, water adsorption and catalytic activity. *Appl. Catal., A* **2011**, *407* (1), 155−162.
(99) Zhou, J.; Zhao, J.; Zhang, J.; Zhang, T.; Ye, M.; Liu, Z. Regeneration of catalysts deactivated by coke deposition: A review. *Chin. J. Catal.* **2020**, *41* (7), 1048−1061.
(100) Rao, K. N.; Venkataswamy, P.; Reddy, B. M. Structural Characterization and Catalytic Evaluation of Supported Copper−Ceria Catalysts for Soot Oxidation. *Ind. Eng. Chem. Res.* **2011**, *50* (21), 11960−11969.
(101) Jeong, H.; Kim, K. I.; Kim, D.; Song, I. K. Effect of promoters in the methane reforming with carbon dioxide to synthesis gas over Ni/HY catalysts. *J. Mol. Catal. A: Chem.* **2006**, *246* (1), 43−48.
(102) Wu, J.; Shen, Y.; Liu, C.; Wang, H.; Geng, C.; Zhang, Z. Vapor phase hydrogenation of furfural to furfuryl alcohol over environmentally friendly Cu−Ca/SiO_2 catalyst. *Catal. Commun.* **2005**, *6* (9), 633−637.
(103) Graciani, J.; Plata, J. J.; Sanz, J. F.; Liu, P.; Rodriguez, J. A. A theoretical insight into the catalytic effect of a mixed-metal oxide at the nanometer level: The case of the highly active metal/CeO_x/TiO_2(110) catalysts. *J. Chem. Phys.* **2010**, *132* (10), No. 104703.
(104) Agnoli, S.; Reeder, A. E.; Senanayake, S. D.; Hrbek, J.; Rodriguez, J. A. Structure and special chemical reactivity of interface-stabilized cerium oxide nanolayers on TiO_2(110). *Nanoscale* **2014**, *6* (2), 800−810.

https://doi.org/10.1021/acsomega.4c02423
ACS Omega 2024, 9, 40394−40410